Revisiting the Causes and Global and Historical Context of the US Midwest Great Flood of 1993

Siegfried D. Schubert[12], Yehui Chang[13], Anthony M. DeAngelis[12], Young-Kwon Lim[14], Randal D. Koster[1], Michael G. Bosilovich[1], Andrea M. Molod[1], Amin Dezfuli[14]

[1]Global Modeling and Assimilation Office, NASA GSFC

[2]Science Systems and Applications, Inc.

[3]Goddard Earth Sciences Technology and Research II / Morgan State University

[4]Goddard Earth Sciences Technology and Research II / University of Maryland Baltimore County (UMBC)

June 17, 2025

Corresponding author:
Siegfried D. Schubert
Science Systems and Applications, Inc.
Lanham, MD USA
siegschu2002@yahoo.com

Revision submitted to the *Journal of Climate*

Abstract

The 1993 US Midwest summer flood occurred in a year marked by a number of apparently disparate climate extremes including an unusually cold spring Pacific warm pool, a record deep spring Aleutian Low, and record wet conditions that spanned the Northern Hemisphere middle latitude land areas during June and July. Here we provide a dynamical framework that links these extremes and accounts for the uniqueness of the Midwest flooding event. In particular, we show that the deep springtime Aleutian low was part of a wave response forced by unusually strong precipitation/heating anomalies in the equatorial Pacific just west of the dateline –heating that was linked to the unusually cold Pacific warm pool juxtaposed to the east with positive SST anomalies tied to a weak but unusually timed El Niño event. The deep springtime Aleutian low in turn produced unusually cold summer North Pacific SSTs and set the stage for the summer's eddy-driven enhancement of the middle latitude jet and unusually strong hemispheric-wide transient (baroclinic) wave activity. The resulting transient vorticity forcing produced two pronounced stationary waves –one in June anchored over northern Eurasia, and another in July anchored over the Pacific/North American region, resulting in record precipitation anomalies over northwestern Eurasia and the Northern Great Plains, respectively.

1. **Introduction**

In 1993 the Midwest U.S. experienced one of the worst flooding events on record. Hundreds of levees along the Mississippi and Missouri Rivers failed, killing 50 people and causing more than $15 billion in damage[1]. Precipitation totals were by far the largest of the 20th century for the 2, 3, 4 and 12 month periods encompassing the 1993 summer (Kunkel et al. 1994), falling on near-saturated soil moisture conditions that already existed throughout the flooding region at the end of March of that year (Climate Analysis Center, 1994).

Bell and Janowiak (1995) carried out a comprehensive observational study of the circulation features that appear to have been key to the main flooding event during June and July. They highlighted the importance of the late May intensification and eastward extension of the North Pacific jet and the July development of a persistent wave pattern over the western and central US. While they suggested that the June/July flooding was largely the result of internal atmospheric variability, they did find observational evidence for a role for El Niño in producing an anomalous springtime North Pacific Pattern (NPP), which helped set the stage for the subsequent active June Pacific storm track.

Numerous studies have addressed the underlying physical processes that caused the flooding. Mo at al. (1995) pointed to the importance of the enhanced transient eddy activity during late May and June that played a key role in strengthening the upper level jet over North America. Trenberth and Guillemot (1996) also found an important role of the jet stream which was displaced well south of the normal location, with high-frequency eddy activity in the Pacific-North American storm track reinforcing the anomalous jet. Liu et al. (1998), employing a linear stationary wave model, found that the 1993 summer circulation anomaly primarily resulted from transient vorticity forcing, in agreement with Mo et al. (1995). They further found the impact of tropical diabatic forcing to be negligible. Weaver et al. (2009) found that the Great Plains low-level jet (GPLLJ) played an important role while soil moisture had only a marginal influence. They determined that both the North Atlantic Oscillation (NAO) and ENSO played a role, with

[1] https://www.livescience.com/7508-history-repeats-great-flood-1993.html

ENSO inducing much of the June large-scale circulation anomaly over the continental U.S. and North Atlantic, while the NAO's influence was largest during July.

While the above studies provide substantial insights into the causes of the 1993 floods, the sequence of events and the underlying dynamical mechanisms leading to the enhanced Midwest precipitation during June and July are still somewhat unclear. Especially unclear is the role of tropical forcing, given that the El Niño event was rather weak[2] and well past its peak by June and July. While it is more likely that it played a role in setting up the spring precursor environment as suggested by Bell and Janowiak (1995), here too it is unclear how such a weak El Niño event produced such a strong spring extratropical response (a record NPP). While there is general agreement that the transient eddies played a role, the changing nature, timing and location of their impacts during the course of the spring and summer is less well established.

Also missing from previous studies is some assessment of the larger (hemispheric) scale context of the floods. In particular, little if anything has been done to address the extent to which the underlying physical mechanisms that produced the Midwest floods also helped produce abnormally wet conditions throughout the middle latitudes of the Northern Hemisphere during that summer. Finally, given that more than 30 years have passed since that flooding event, we can make a new assessment of just how unique (and extreme) that flooding event really was.

Our focus is on June and July of 1993 – the two months during which the excessive Midwest precipitation anomalies were responsible for the most extreme flooding that occurred over the US Midwest. An additional focus is on the springtime (March to May, MAM) anomalies that helped set the stage for the subsequent summer extreme circulation and precipitation anomalies. As described in Section 2, our approach to assessing the underlying forcings involves the use of atmospheric general circulation model (AGCM) experiments, supplemented with results from a stationary wave model (SWM) and coupled model retrospective seasonal forecasts. Results are presented in Section 3, and conclusions are presented in Section 4.

[2] https://origin.cpc.ncep.noaa.gov/products/analysis_monitoring/ensostuff/ONI_v5.php

2. The Model Experiments

a. The GEOS AGCM and replay experiments

The AGCM experiments (e.g., Schubert et al. 2019b; 2021) are conducted with the NASA Goddard Earth Observing System (GEOS) model (Molod et al. 2015) applying a "regional replay" approach, in which the atmosphere is constrained to remain close to the NASA Modern Era Retrospective-Analysis for Research and Applications, Version 2 (MERRA-2, Gelaro *et al*. 2017) over specified regions of the globe. Simply put, within the defined replay region, the atmospheric state (in terms of the prognostic variables: temperature, specific humidity, horizontal winds, surface pressure) is forced to match the reanalysis during a simulation; outside of the replay region, on the other hand, the atmosphere is allowed to evolve freely. We can thereby determine the remote impacts of the replay region's behavior on the rest of the globe (e.g., Schubert et al. 2022; DeAngelis et al. 2023; Schubert et al. 2024).

The model equations governing replay were outlined by Chang et al. (2019). Their general form is: $\frac{\partial x}{\partial t} = f(x) + \Delta x$, where $\Delta x = (\text{analysis} - \text{forecast})/6\text{hrs}$, and where f(x) captures the effects of all the model's dynamics and physics terms. We recompute Δx every 6 hours but apply it at each time step, appropriately scaled. The GEOS AGCM used here is basically the same as that underlying MERRA-2 except for two important features: (i) here we run it at a coarser horizontal resolution (approximately 1°, compared to 1/2° for MERRA-2), and (ii) our application of the AGCM includes a tendency bias correction (TBC) term, one that reduces some of the model's long-term biases (Chang et al. 2019)[3].

Table 1 provides the details of our 45-member ensembles of AGCM replay runs, all of which are forced by observed SST. This includes a set of runs without any replay region (referred to as no-replay, NORPL) and another set in which the tropics is constrained (RPL_TR), addressing both the impact of SST and other potential tropical forcing. Both NORPL and RPL_TR ensemble

[3]The TBCs are essentially 6-hourly analysis increments (first guess forecast minus analysis) time-averaged over multiple decades. The increments were obtained from MERRA-2 reanalysis data. The TBCs are added with opposite sign as additional forcing terms to the model equations. See Chang et al. (2019).

members were initialized in 1981 and run through 2023. Our choices for the remaining replay regions (central North Pacific: RPL_CNP; North America/North Atlantic: RPL_NA, and tropical central Pacific: RPL_TCP) address more localized potential forcing regions, as justified in subsequent sections. To reduce the computational burden, these sets of 45-member replay runs (RPL_CNP, RPL_NA, and RPL_TCP) are much shorter in length - they were initialized on either 1 January 1993 or 30 Nov 1992 (see Table 1) and run through the summer of 1993. However, in order to produce climatologies for those replay regions, a single ensemble member spanning 1991-2020[4] was produced for each. For consistency, the climatologies for both NORPL and RPL_TR were also based on a single ensemble member spanning those years.

Table 1: List of the AGCM experiments discussed in the text. All runs are forced with observed daily mean SST (see Gelaro et al. 2017 for details about the SSTs). The perturbations to the initial conditions for each of the ensemble members were produced by taking the differences between two atmospheric states separated by one day, scaling those differences by 1/8, and adding them to (or subtracting them from) the initial state. NORPL, RPL_TR and RPL_NA were initialized from MERRA-2, while RPL_CNP and RPL_TCP were initialized from NORPL. Further information about that approach to perturbing initial conditions can be found in Schubert et al. 2019a.

Name	Time period	Replay region	Ensemble members
NORPL	1981-2023	none	45
RPL_TR	1981-2023	Tropics: 25°S-25°N	45
RPL_CNP	1 Jan 1993 – 31 Aug 1993	Central North Pacific: (25°N-70°N, 150°E-150W°)	45
RPL_NA	30 Nov 1992 – 31 Aug 1993	North America/North Atlantic: (25°N-70°N, 90W°-30W°)	45
RPL_TCP	1 Jan 1993 – 31 Aug 1993	Tropical Central Pacific: 25°S-25°N, 150E°-150W°)	45

b. *The Stationary Wave Model Experiments*

Simulations with a stationary wave model (SWM) were used to isolate further the relevant forcing regions and thereby help us understand the replay results. The SWM is essentially the

[4] For computational efficiency, each year of the climatology was run as a separate simulation, initialized on May 31 of the prior year (year -1) and run through the end of that year (year 0).

dry dynamical core of a full AGCM; a rhomboidal wavenumber-30 truncation is used in the horizontal, and 14 unevenly spaced σ levels are used in the vertical (Ting and Yu 1998).

Our analysis will focus on numerous SWM simulations performed with imposed idealized heating or vorticity sources (following the examples of Schubert et al. [2011] and DeAngelis et al. [2023]). The idealized heat or vorticity forcing is imposed at forcing locations spaced every 10° longitude and 5° latitude across the globe (one location per simulation). These idealized forcing sources have a sine-squared functional spatial structure; for vorticity, a horizontal scale of 10° longitude by 10° latitude is applied, whereas for heat, the applied scale is 40° longitude by 10° latitude. Regarding the imposed forcing's vertical structure (see Liu et al 1998), that for vorticity peaks in the upper troposphere (with a value of ~5.4 x 10^{-10} s^{-1}) and that for the heating is highest in the middle troposphere (with a value of ~3.1°K day^{-1}).

To summarize such a large collection of simulations in a way relevant to the observed circulation anomaly of interest, Schubert et al. (2024) describe an approach that identifies those forcing locations for which the response projects most strongly on our phenomenon of interest – our observed target anomaly pattern. We refer to those identified forcing locations as a "forcing sensitivity map", expressed as a vector (**s**). In essence, the values in **s** represent the extent to which each SWM response (to either vorticity or heat forcing at a particular location) resembles the observed pattern. This sensitivity map can provide insight into the forcing regions that are most relevant to a particular target anomaly. We supplement this map with various MERRA-2-based estimates of the actual forcings, noting that the most likely forcing for a particular observed circulation anomaly occurs where the actual forcing coincides with a region showing large sensitivity in the SWM-based map.

Vorticity forcing is examined in terms of the transient vorticity flux convergence, which can be written as (Wang and Ting 1999; DeAngelis et al. 2023):

$$\mathrm{TF}_{\mathrm{vor}} = -\nabla \cdot \overline{\mathbf{V}'\zeta'}. \qquad (1)$$

Here, **V** is the horizontal wind vector, and ζ is the vorticity. The overbar represents a monthly mean, and primes represent instantaneous (6-hourly) deviations from that mean. Typically associated with weather disturbances, this vorticity forcing has been shown (e.g., Schubert et al. 2011, DeAngelis et al. 2023) to force northern midlatitude stationary Rossby waves. We compute it here from MERRA-2 6-hourly data, applying an inverse Laplacian operator to better isolate, through spatial filtering, its broader aspects (e.g., Schubert et al. 2011). Observed diabatic heating anomalies (derived from MERRA-2 data, as described in DeAngelis et al. 2023) are also examined here.

c. *The GEOS S2S V2 model seasonal forecasts*

We supplement our analysis with an examination of selected retrospective seasonal forecasts (hindcasts) performed with the GEOS S2S V2 coupled model (Molod et al. 2020). Chief components of this S2S system include the GEOS AGCM [Molod et al., 2015; Rienecker et al., 2008], the Modular Ocean Model-5 (MOM5) ocean general circulation model [Griffies et al., 2005; Griffies, 2012], and the Catchment land surface model [Koster et al., 2000]. The AGCM was run at a spatial resolution of ~0.5°, with 72 hybrid sigma/pressure levels in the vertical, while the ocean model was run at ~0.5° spatial resolution, using 40 vertical layers extending to a depth of 4500 m.

GMAO seasonal forecasts are initialized on a fixed set of calendar dates, five days apart beginning on 1 January. For the retrospective seasonal forecasts, the start dates form a lagged ensemble of four for any month. After 2016 (when the system started producing real-time forecasts), we use only the unperturbed forecasts initialized every five days (despite the larger ensemble size) to be consistent with the earlier retrospective forecasts. The climatology used to compute anomalies is based on forecasts spanning 1991–2020. Further details about the forecast procedure and initial conditions can be found in Molod et al. (2020).

3. Results

We begin in Section 3a with a brief review of the observed 1993 spring and summer anomalies, together with an assessment of just how unusual those anomalies were. Section 3b examines the development of the 1993 MAM anomalies, focusing on the results from the GEOS AGCM simulations, as well as some limited supporting results from the GEOS coupled model predictions. Section 3c examines the subsequent development of the unusually strong summer (June/July) jet, including the feedbacks with transient and stationary wave activity. We then look more closely at the causes of the main precipitation-producing circulation anomalies that developed over western Eurasia in June (Section 3c1) and over North America in July (Section 3c2).

a. The Observed Anomalies

Figure 1 underscores the exceptional nature of the June/July 1993 precipitation anomalies in the NH extratropics. In addition to the extreme precipitation that fell over the northern Great Plains, much of the land area (particularly in western Eurasia) between about 30°N and 60°N (Fig. 1a) was anomalously wet. Figure 1b shows that 1993 had, by far, the largest positive June/July precipitation anomaly (averaged over land between 30°N-60°N) of the last four decades.

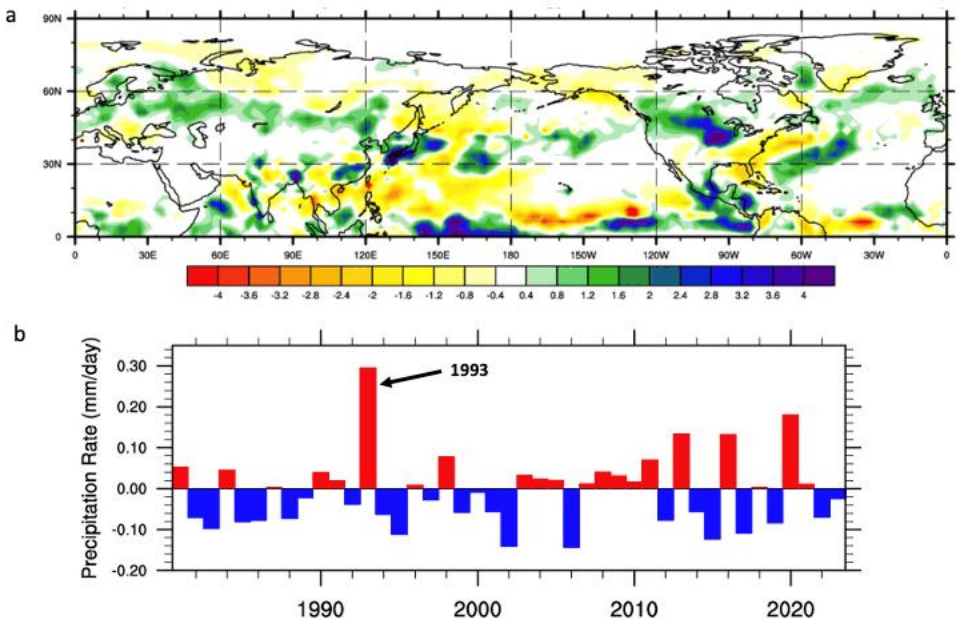

Figure 1: a) The 1993 June to July Northern Hemisphere precipitation anomalies. b) The zonal-mean (land only) June to July precipitation averaged between (30°N-60°N) for 1981 through 2023. Units: mm day^{-1}. The precipitation data are from GPCP V2.3 (Adler et al. 2016). The climatology used to produce the anomalies spans the years 1991-2020. Images provided by the NOAA-ESRL Physical Sciences Laboratory, Boulder Colorado (Smith et al. 2014) from their Web site at https://psl.noaa.gov/.

Some insight into the possible causes of the very wet conditions throughout the NH middle latitudes can be gained by examining the daily evolution of the 250 hPa meridional wind anomalies (left panel of Fig. 2). Several remarkable changes in the character of the anomalies are outlined by the heavy black lines. Overall, we see a general tendency for enhanced eastward (synoptic time scale) wave propagation (quantified in Section 3c), with two exceptional periods/regions for which more stationary disturbances clearly tend to develop. The latter occurs over the western Eurasian region primarily during June (box b) and over North America during July (box e). These circulation features are reflected in the precipitation anomalies (right panel of Fig. 2), where both the anomalous eastward propagation and the more stationary nature of the enhanced precipitation (over western Eurasia and North America) are clearly evident.

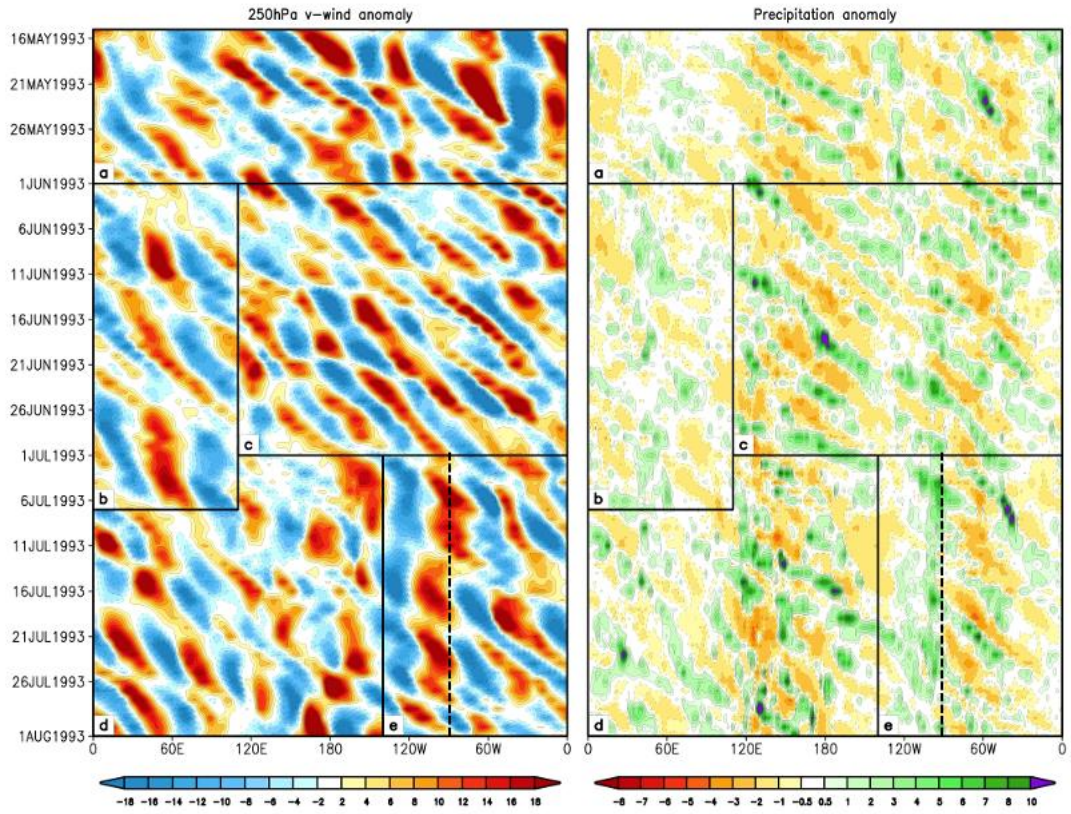

246

247 Figure 2: Left panel: Hovmoller (time/longitude) plot of the daily 250 hPa meridional wind (v-
248 wind, m/s) anomaly averaged between 35°N-70°N for the period May 15 to July 31, 1993. Right
249 panel: Same as left panel but for precipitation (mm/day). The heavy black lines serve to roughly
250 highlight the times and longitudes (labeled a – e) of different behavior manifest in the v-wind
251 anomalies with boxes (b) and (e) specifically encompassing the longitudes and times of quasi-
252 stationary behavior over western Eurasia during June, and North America during July,
253 respectively. The dashed lines in e indicate 90°W. Results are from MERRA-2, though the
254 precipitation used for verification is an observationally corrected product (Reichle et al. 2017).

255

256 With an eye towards possible tropical connections to these extratropical anomalies (addressed in
257 the following sections), we next look into the unusual state of the tropical Pacific SST during the
258 1993 boreal spring and how that impacted the extratropics. This is motivated by the observational
259 study of Bell and Janowiak (1995) that pointed to the extreme positive phase of the North Pacific

pattern (NPP) during MAM[5] as likely setting the stage for the extremely active Pacific storm track that eventually (in June) extended into the U.S., contributing to the wet conditions there.

Fig. 3a shows that the overall pattern of the MAM 1993 SST anomalies were not dissimilar to those of an El Niño event, though the eastern tropical Pacific positive anomalies were rather weak, and the warm pool anomalies were unusually cold (the coldest of the last 4 decades – not shown). The warm eastern Pacific tropical SST anomalies in fact reflect a weak but unusually timed (peaked in May) El Niño that appears to have been initiated by a strong January 1993 MJO (Delcroix et. al. 2000; see also S1 showing the daily evolution of the SST and related tropical Pacific anomalies). The 250 hPa height anomalies during that spring (Fig. 3b) were characterized by a pronounced negative anomaly in the North Pacific reflecting, in the upper troposphere, the extreme state of the NPP.

To put the above SST anomalies in historical context, we show in Fig. 3c the time series of the MAM tropical Pacific SST averaged over the western Pacific minus the average over the eastern Pacific for the period 1981-2023. We choose such an east/west difference metric with the understanding that changes in the SST zonal gradient are especially relevant for driving an atmospheric response (e.g., Lee et al. 2022). Here we see that the largest negative values of the anomalous gradient occur during 1992 (an El Niño year) and 1993, reflecting in part the unusually cold warm pool that developed during those two years - apparently as a lingering impact of the June 1991 Pinatubo eruption (Ward et al. 2021). Looking across the entire record, we see a general tendency for the anomalous gradient to be negative during the 1980s and 1990s, with a change to generally positive values after that. This appears to reflect a climate shift that occurred in the Pacific SST during boreal spring in 1998-99 linked to a low frequency mode of variability resembling the Pacific Decadal Oscillation (Lyon et al. 2014).

Fig. 3d shows the time series of the 250 hPa height anomalies averaged over a region spanning the North Pacific (see the box in Fig. 3b). This region was chosen to be consistent with that used by Trenberth and Hurrel (1994) to define the North Pacific Index (NPI) – a simpler version of the NPP. The spring of 1993 stands out as having the largest negative anomaly, although the negative

[5] The NPP pattern in Bell and Janowiak (1995) is based on a rotated principal component analysis, with a positive value indicating negative SLP anomalies in the North Pacific.

1992 anomaly is also relatively large. It is worth noting that the summer of 1992 was also wet in the US Midwest (not shown), though not nearly as extreme as the summer of 1993. Looking over the entire record, the general character of the height anomalies is similar to that of the SST gradient (cf. Figs. 3c and d) with generally negative values during the 1980s and 1990s, and a change to generally positive values after that, again apparently reflecting the climate shift mentioned above. While the North Pacific height anomalies are known to exhibit a substantial amount of internal variability unforced by SST (e.g., Zhang et al. 2018), these results are nevertheless suggestive of a substantial tropically forced component – something we will address in the next section focusing on 1993.

To summarize, the results in Fig. 3 provide some insight into the unusual state of the tropics in the Pacific during MAM of 1993: a strong zonal gradient in the SST resulting from the juxtaposition of an unusually cold Pacific warm pool and a weak but unusually timed El Niño (peaked in May), occurring within a tropical Pacific climate regime (which ended in 1998/99) that appears to favor a negative upper tropospheric height response in the North Pacific.

We next use our GEOS AGCM replay experiments and the GEOS coupled model predictions to investigate the tropical forcing that produced the particularly large atmospheric response in the North Pacific during MAM 1993, and how that acted to set the stage for the unusually wet conditions that developed in the NH extratropics during the following June and July.

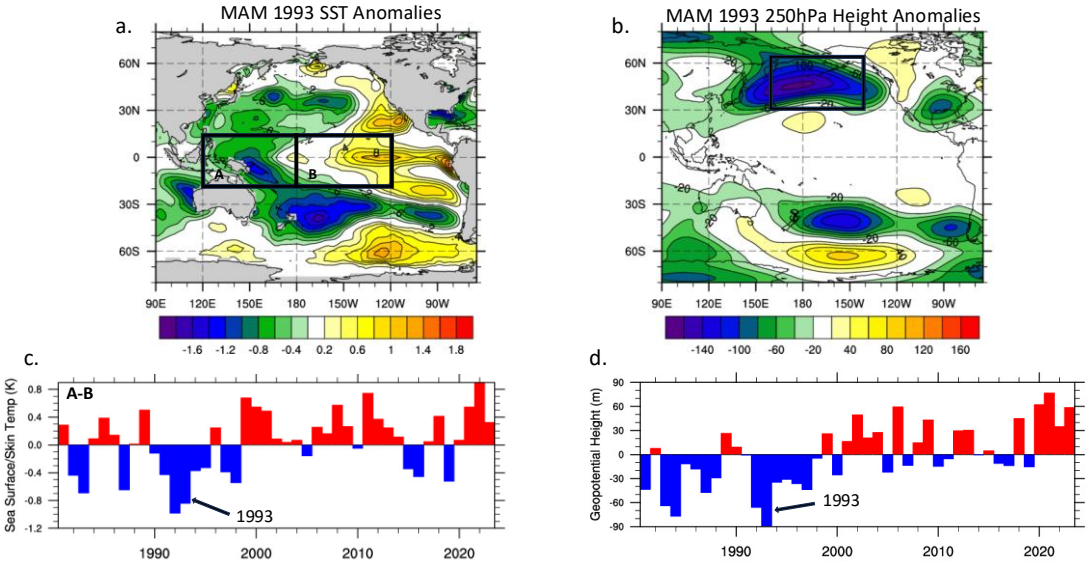

305

306 Figure 3: a) The 1993 March to May (MAM) average SST anomalies (°C) from NOAA ERSST
307 V5. b) The 1993 MAM average 250hPa height anomalies (m) from MERRA-2. c) The MAM
308 average SST anomaly (°C) averaged between (15°S – 15°N, 120°E-180°E) minus the SST
309 anomaly (°C) averaged between (15°S – 15°N, 180°E-120°W), for 1981 through 2023 (see boxes
310 A and B in panel a). d) The MAM 250hPa height anomaly (m) averaged between (30°N– 65°N,
311 160°E-140°W) for 1981 through 2023 (see box in panel b). The climatology used to produce the
312 anomalies spans the years 1991-2020. Images provided by the NOAA-ESRL Physical Sciences
313 Laboratory, Boulder Colorado from their Web site at https://psl.noaa.gov/.

314

315 b. The 1993 spring (MAM) precursor developments

316 Figure 4 shows the MAM 1993 precipitation, 250hPa stream function (ψ), and sea level pressure
317 (SLP) anomalies from MERRA-2 and our NORPL and tropical replay simulations. The MERRA-
318 2 results show quite clearly the signatures of the extreme negative NPI in the SLP anomalies (Fig.
319 4l). The upper tropospheric ψ anomalies (Fig. 4k) show a North/South dipole pattern in the
320 western North Pacific (something that is less evident in the height anomalies shown in Fig. 3b)
321 apparently emanating from the region of excessive precipitation just west of the dateline, with the
322 negative pole directly above the anomalous deep Aleutian low which extends across the entire
323 length of the North Pacific basin.

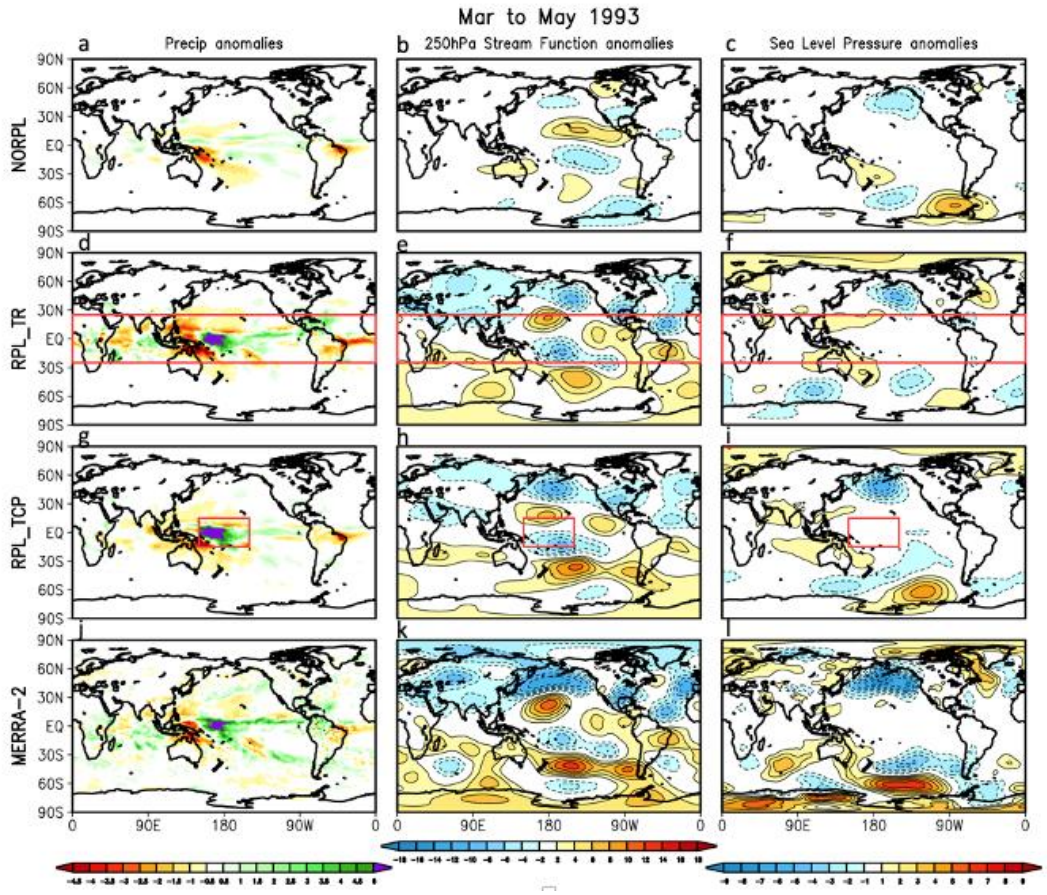

Figure 4: Left panels: Precipitation anomalies (mm/day). Middle panels: The 250 hPa stream function (ψ) anomalies (10^6 m^2/s). Right panels: Sea level pressure anomalies (hPa). The results are from top to bottom for NORPL, RPL_TR, RPL_TCP, and MERRA-2. All results are March to May 1993 averages, and all model results are the ensemble means. The red boxes indicate the replay regions. The climatology used to produce the anomalies spans the years 1991-2020. The MERRA-2 precipitation is an observationally corrected product (Reichle et al. 2017).

The RPL_TR simulations (Figs. 4d-f) show somewhat similar anomalies in the North Pacific (for both ψ and SLP) though weaker and less extensive in the east/west direction. The tropical precipitation anomalies are of course largely reproduced by design, though it is worth remembering that replay does not directly constrain the precipitation. Notice that the anomalies are considerably different from those of NORPL (Figs. 4a-c). In particular, the ψ anomalies in NORPL in the North Pacific are weaker and mostly confined to the eastern subtropical North

Pacific, with a considerably weaker SLP anomaly. The precipitation anomalies in the tropical Pacific are also quite different, showing little signature of the positive anomaly west of the dateline; only weak positive anomalies are seen, largely confined to the eastern tropical Pacific (Fig. 4a). It thus appears that the NORPL ψ anomalies are a response to the weak eastern tropical Pacific surface heating. To confirm that the RPL_TR results mostly reflect the response to the heating near the dateline, we show in Figs. 4g-i the results of replaying a much smaller tropical region (RPL_TCP) that just encompasses the main positive precipitation anomaly. We see that much of the RPL_TR response is indeed reproduced in those runs.

It is important here to point out that there is considerable variability in the MAM atmospheric response in the North Pacific even if the tropics are essentially perfectly known. This is illustrated in Fig. 5 which shows the results (250hPa stream function and SLP anomalies averaged over the North Pacific region in Fig. 3b) for the individual ensemble members from RPL_TR. Here we see that while the impact of replaying the tropics is to shift the ensemble mean values towards the observed (MERRA-2) values (see also Figs. 4e and f), there is considerable intra-ensemble variability in the results, reflecting the internal (unforced by SST) atmospheric variability in the North Pacific. As such, the RP_TR results should be interpreted probabilistically. That is, we need to consider both the shift in the ensemble mean and the ensemble spread in telling us about the extent to which the tropical forcing increased the probability of the observed value occurring.

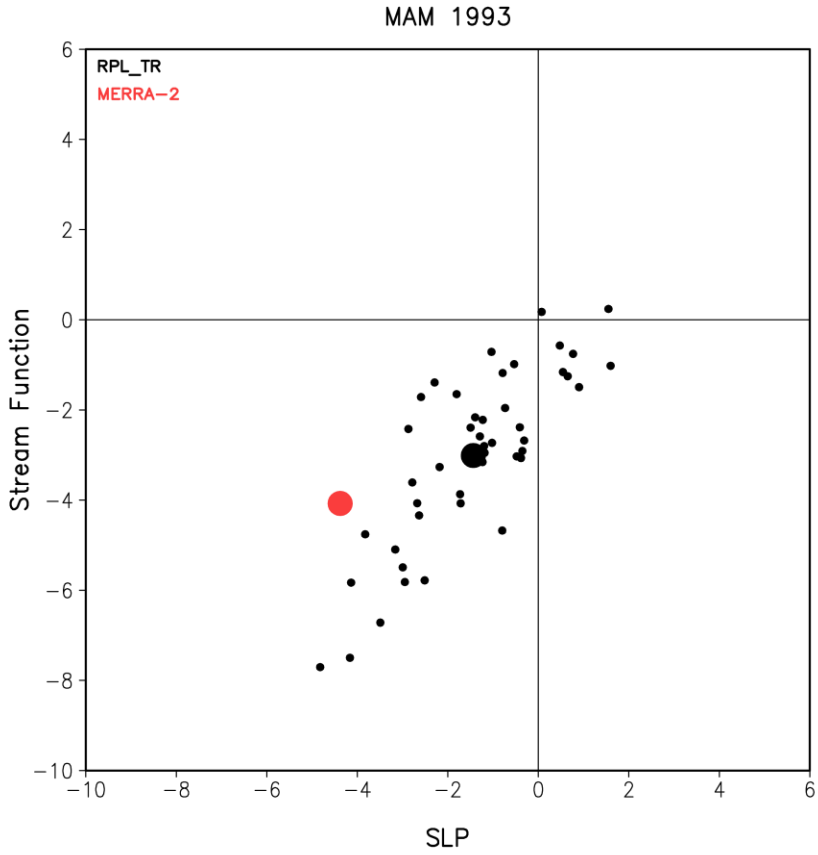

357

358 Figure 5: Scatterplot of the 1993 MAM 250 hPa stream function (ψ) anomalies (10^6 m^2/s) versus
359 the sea level pressure anomalies (SLP, hPa) averaged over the region (30°N– 65°N, 160°E-
360 140°W). The small black dots are the individual ensemble members from RPL_TR. The large
361 black dot is the ensemble mean. The red dot indicates the MERRA-2 values.
362

363 Given the key role of that tropical precipitation anomaly just west of the dateline in forcing the
364 extratropical response, it is important to understand why it is not reproduced in the NORPL runs.
365 In fact, none of the 45 NORPL simulations (runs that are forced with the observed SST) produce
366 positive tropical precipitation anomalies west of the dateline anywhere close to the observed
367 (MERRA-2) amplitude (not shown). Assuming 45 ensemble members are sufficient to sample the
368 spread of the possible outcomes and that the AGCM is not deficient, this suggests coupling to the
369 ocean may be important. To address this, we next turn to our GEOS S2S-2 model hindcasts.

Fig. 6 shows that coupling with the ocean does indeed appear be important for generating the observed tropical (precipitation) and extratropical response as highlighted by a remarkably skillful MAM hindcast produced with the GEOS S2S-2 coupled model from the January 16 initial conditions (cf. the first and second columns of Fig. 6). This is one of 8 hindcasts initialized every 5 days during January and February 1993 (see Section 2c). This result, however, is not robust; we performed 10 additional simulations by perturbing[6] the January 16 initial conditions and found that the relatively small perturbations to the initial conditions leads to quite different outcomes (the last column of Fig. 6 shows the ensemble mean). We look at all 8 hindcasts initialized in January and February 1993 in section S2. Based on those results, we speculate (and provide some evidence in section S2) that the observed atmospheric response to those SST anomalies appears to reflect one of two possible Bjerknes feedback regimes, with the other characterized by an atmospheric response largely confined to the eastern North Pacific – something more typical of a medium to strong El Niño event. With so few cases (8) we are unable to assess what, if anything, in the initial conditions leads to one or the other regime, underscoring the challenge of predicting this key precursor to the summer flooding. Nonetheless, that the coupled model shows a more realistic response to the SSTs in at least a few members (compared to no members from the AGCM), again demonstrates the likely importance of coupling

[6] Here we perturb only the atmosphere (not the ocean), employing the same approach used to generate perturbations for the replay runs as described in Table 1 of the main text.

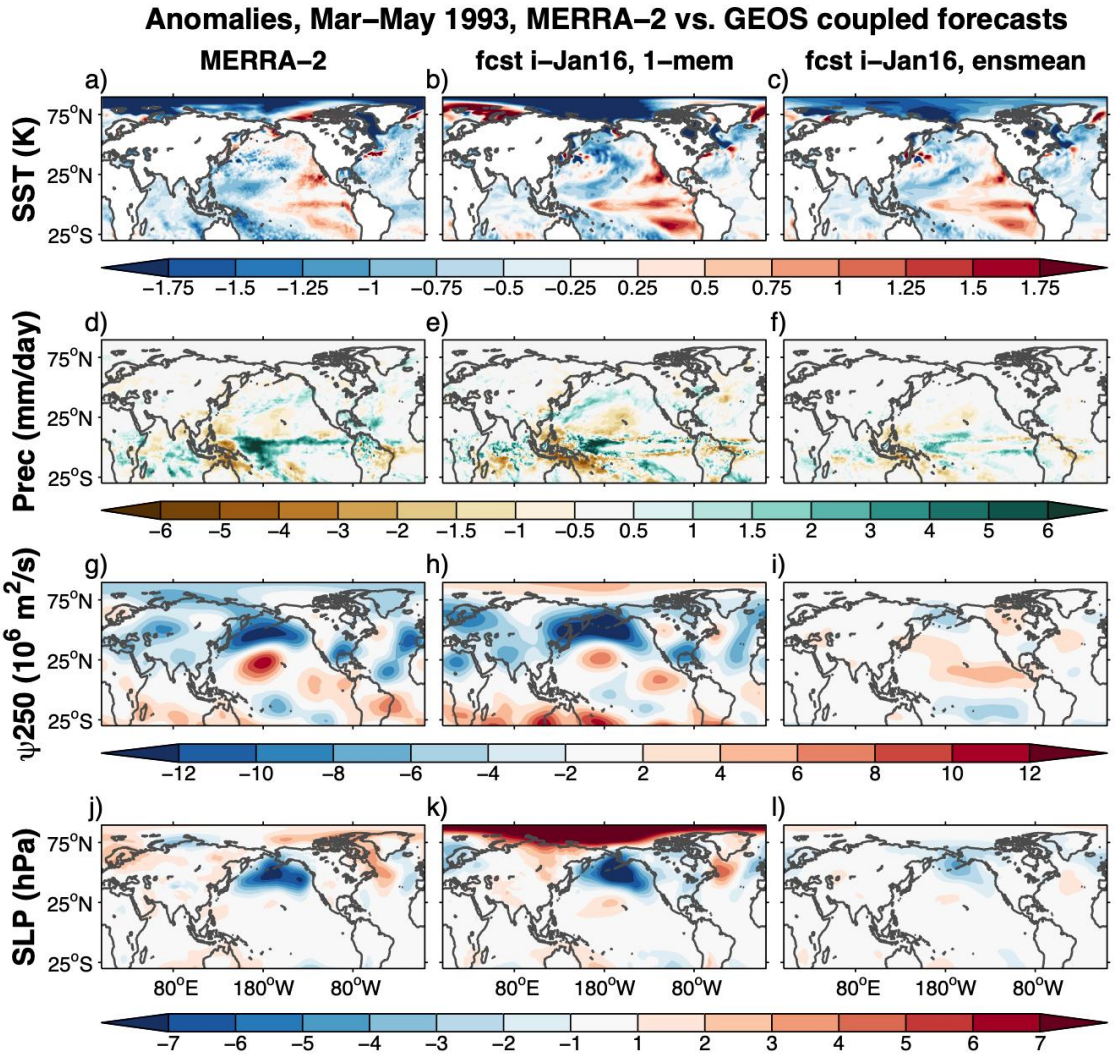

Figure 6: Selected MAM 1993 results from MERRA-2 and GEOS-S2S-2 coupled model hindcasts. The results (anomalies) are from top to bottom, SST (K), precipitation (mm/day), 250 hPa stream function ($\psi 250$, $10^6 m^2/s$) and sea level pressure (SLP, hPa). The first column is from MERRA-2, the second column is from a GEOS-S2S-2 coupled prediction initialized on January 16, and the third column is the ensemble mean results from an 11-member suite of hindcasts initialized by perturbing the January 16 initial conditions.

c. The Summer (June and July) Anomalies

As noted in the Introduction, previous studies have highlighted the importance of the enhanced and equatorward-shifted North Pacific jet and a vigorous storm track that extended in the US

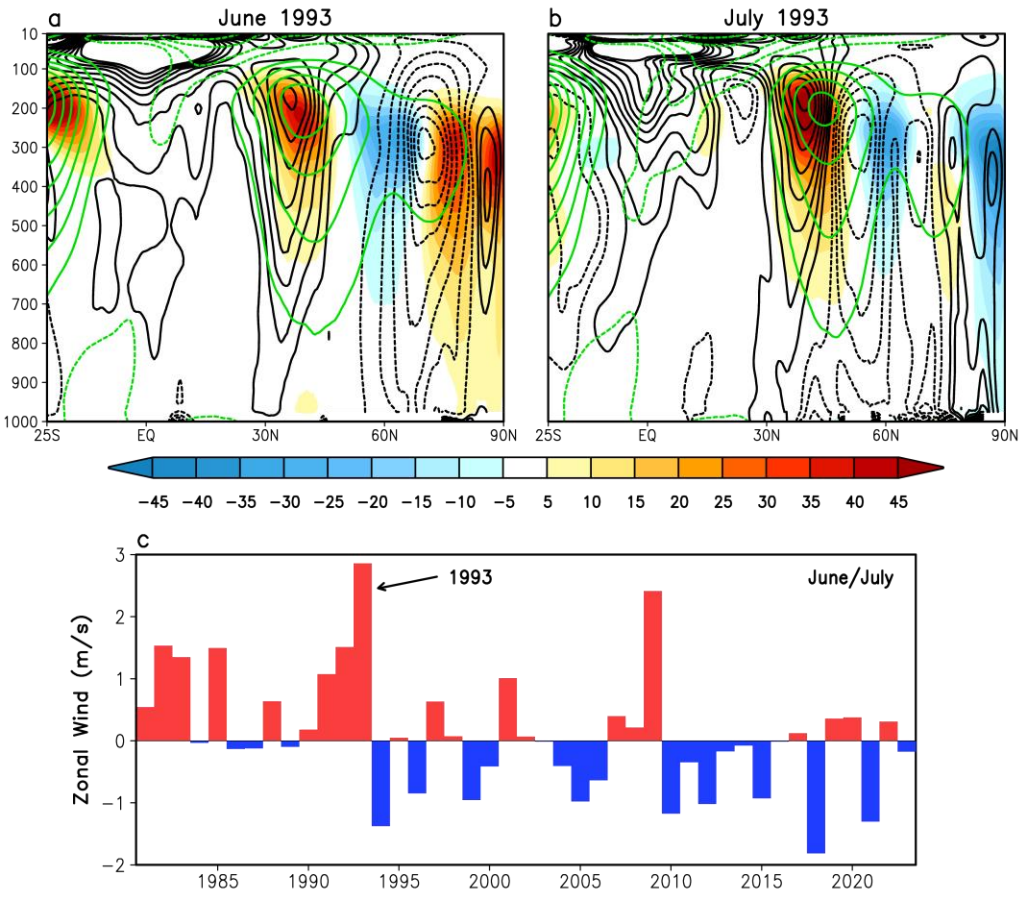

399

400 Figure 7: a) The June 1993 zonal-mean u-wind anomalies (black contours, every 0.5 m/s,
401 negative dashed and zero omitted) with superimposed anomalous zonal-mean v-wind squared
402 associated with the transient eddies ($[\overline{v^{*\prime}v^{*\prime}}]$, shaded, m^2/s^2). Green contours are the
403 climatological zonal-mean u-winds, with contours every 5 m/s (negative dashed and zero
404 omitted). b) Same as (a) but for July 1993. c) The June to July 250mb zonal-mean u-wind
405 averaged between 35N and 45N for the period 1981 through 2023. The climatology used to
406 produce the anomalies spans the years 1991-2020. Results are from MERRA-2.
407

408 Midwest during June, contributing to the wet conditions there. Figures 7a and 7b show that the jet
409 enhancement, its equatorward shift, and enhanced storm track (transient eddy activity[7]) have
410 signatures in zonal-mean statistics. The anomalous transient eddy activity is, during both months,
411 positive in the latitudes where the jet is enhanced (between 30°N-45°N), and negative in the

[7] As a measure of synoptic storm activity, we define transient eddy activity as $[\overline{v^{*\prime}v^{*\prime}}]$, where v is the meridional wind, the asterisk is the eddy or deviation from the zonal mean, prime is the instantaneous 6-hourly deviation from the monthly mean, overbar is the monthly mean, and bracket is the zonal mean.

latitudes of negative zonal wind anomalies centered at about 60°N. The unusual strength of the jet is highlighted in Fig. 7c, which shows that the 1993 June/July middle latitude zonal-mean u-wind anomalies in the upper troposphere have not been surpassed in strength in the last four decades, though it is noteworthy that part of that value (about 10%) appears to be related to a trend that acts to decrease the values in the later years.

The above summer zonal-mean anomalies appear to reflect, in part, the persistence of the springtime anomalies in the North Pacific associated with the record NPI, with the cold tropospheric temperatures (between 30°N-60°N) persisting into the summer (cf. Figs. S3a,b). In addition, those cold temperatures were supported by a band of unusually cold SST anomalies spanning much of the North Pacific between 30°N and 40°N that developed as a result of the strong MAM surface westerlies linked to the record deep Aleutian low (Figs. S3c,d). Those cold SSTs presumably acted to feedback on the atmosphere supporting the development of an enhanced North Pacific jet. However, understanding what produced the hemispheric-wide changes in the jet and eddy activity requires an assessment of the feedback between the eddies and the zonal-mean u-wind. A useful diagnostic in that regard is the Eliassen-Palm (E-P) flux (Eliassen and Palm 1961) which quantifies the contribution of the eddies (deviations from the zonal mean) to the zonal-mean zonal momentum budget. This can be written as (Edmon et al. 1980):

$$\frac{\partial [u]}{\partial t} \approx (a\,cos\varphi)^{-1} \nabla \cdot \boldsymbol{F} \ , \qquad (2)$$

where **F** is the E-P flux vector with components

$$F_{\varphi} = -a\,cos\varphi [u^{*} v^{*}] \qquad (3a)$$

$$F_{p} = f a\,cos\varphi [v^{*} \theta^{*}] / \left[\theta_{p}\right]. \qquad (3b)$$

439 In the above, the brackets represent a zonal mean, and asterisks the deviations from the zonal
440 mean. Also, a is the radius of the Earth, f is the Coriolis parameter, φ is latitude, θ is potential
441 temperature, p is pressure, and (u,v) are the zonal and meridional wind components.
442
443 Fig. 8 shows the E-P fluxes and flux divergence superimposed on the u-wind anomalies for June
444 (left panels) and July (right panels) 1993. Here, the time averaged quadratic (E-P flux) terms
445 have been decomposed into contributions from the stationary and transient eddies. During June,
446 the upward flux between 40-50°N associated with the transient eddies (Fig. 8a) reflects the
447 developing baroclinic waves (Edmon et al. 1980) which, as they diverge in the middle and upper
448 troposphere, act to support the positive u-wind anomalies in the mid-troposphere centered on
449 30°N and north of about 40°N. On the other hand, it is primarily the downward and poleward E-
450 P flux associated with the stationary eddies that support the main positive zonal-mean u-wind
451 anomalies in the upper troposphere between 30-40°N (Fig. 8b). Those stationary eddies, while
452 not particularly strong, appear to be trapped within the jet wave guide throughout the hemisphere
453 between about 25°N – 45 °N (Fig. 10a), acting collectively to both strengthen and shift the
454 zonal-mean jet equatorward. Stationary eddies also appear to be the primary drivers of the main
455 negative u-wind anomaly between 60-80°N (Fig. 8b), though that is partly compensated for by
456 the transient eddies (Fig. 8a). Those stationary eddies are located primarily over northern
457 Eurasia (Fig. 10a) – our focus in Section 3.c.1. We note that the above negative zonal wind
458 anomalies (see also those for July in Fig. 8e) contribute to narrowing the meridional jet profile
459 and producing the double jet structure that appears to be an important factor in facilitating quasi-
460 resonance (Petoukhov et al. 2013).
461
462 During July, it appears again that the main support for the positive u-wind anomalies between
463 about 25-40°N is provided by the stationary eddies with E-P fluxes that are directed poleward
464 and downward (Fig. 8e), thereby again acting to both strengthen and shift the jet equatorward.
465 The stationary eddies are also trapped within the jet wave guide though in July they are primarily
466 located over the North Pacific/North American region (Fig. 13a): our focus in Section 3.c.2.
467 While the impact of the transient eddies is spatially rather noisy (Fig. 8d), they reinforce the
468 stationary waves upper tropospheric impact between 50°-60°N to enhance the negative u-wind
469 anomalies there (Fig. 8f).

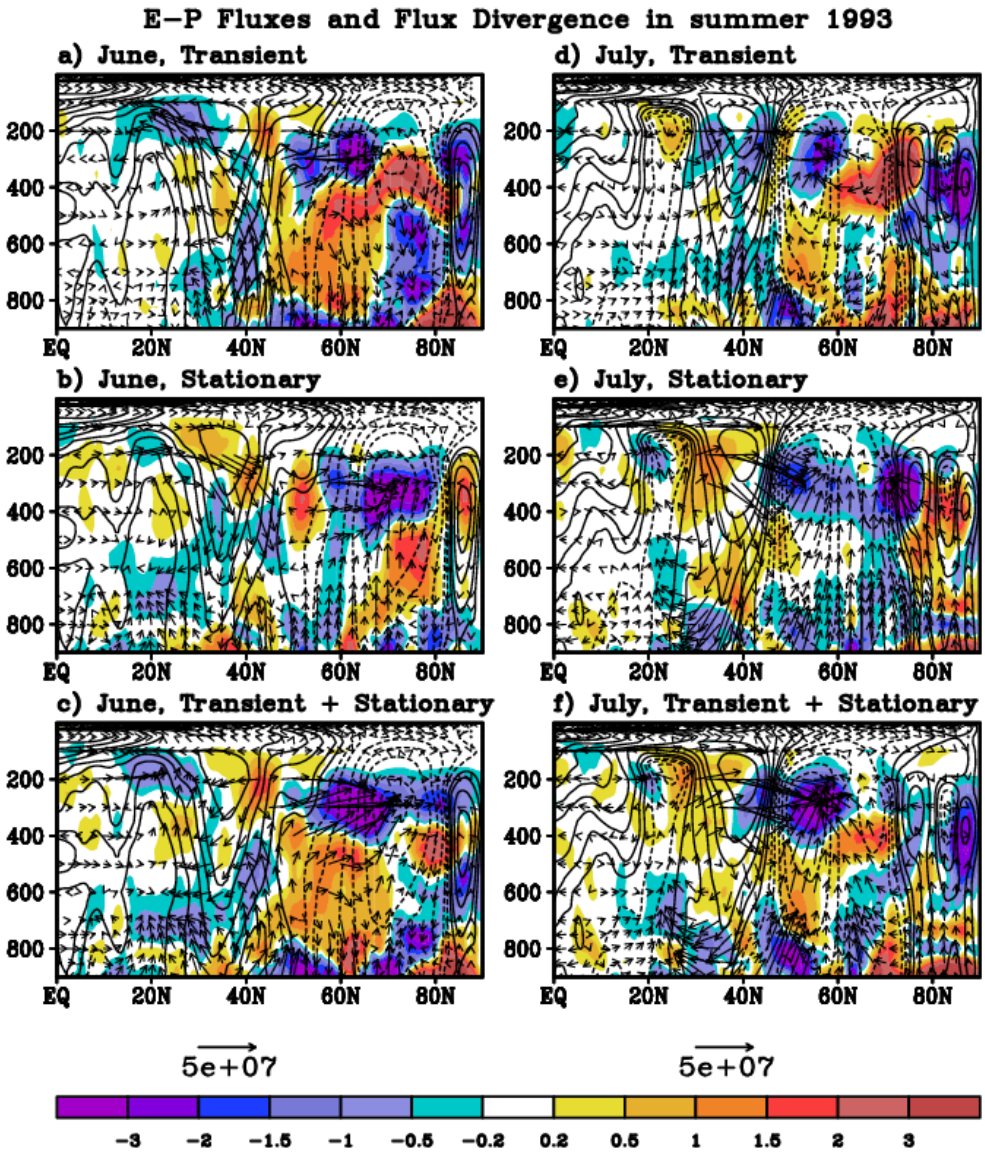

Figure 8: Zonal-mean dynamics for June (left panels) and July (right panels) 1993 based on MERRA-2. Top panels: The anomalous transient eddy E-P flux (F, vectors) and divergence of F (shaded, m/s day^{-1}). The transient fluxes are computed from instantaneous 6-hourly deviations of the relevant quantities from the monthly mean. Middle panels: Same as top panels but for the stationary eddies. Bottom panels: Same as top panels but for the transient plus stationary eddies. The contours are the u-wind anomalies, drawn at 0.2, 0.5, 1, 1.5, 2, 3, 4, 6, and 8 m/s with negative contours dashed.

Here, it is important to note that the summertime hemispheric-wide expansion of the eddy activity is facilitated by the climatological annual cycle of the zonal winds, which results in (even in the absence of any anomalous forcing) a longitudinally more uniform wave guide for the eddies (waves) to propagate around the globe during summer, compared with spring when the waveguide is more limited in extent since the strongest zonal winds are largely confined to the western North Pacific (not shown). In summary, the anomalous summer (June/July) jet enhances the wave activity and is itself enhanced by the wave activity, representing a feedback. Specifically, the jet enhances transient eddy activity, the transient eddies help force stationary eddies (see below), and then both transient and stationary eddies feed back on the jet.

We next examine the pronounced stationary waves that developed over the eastern hemisphere (0°-120°E) in June, and over the North Pacific/North American region (150°W – 60°W) in July (Fig. 2). While our main focus is on the northern Great Plains (our flood region) in July, a brief look into the causes of the June extreme precipitation event over western Eurasia (with details in section S4) helps to underscore the hemispheric-scale controls of the unusually strong stationary and transient eddy activity during those two months.

c1. The June event

Figure 9 shows that the overall wet conditions that occurred throughout the NH middle latitude land areas averaged for June and July (Fig. 1) is already clearly evident in June. In addition to the wet conditions over the U.S. northern Great Plains tied to the active storm track (Fig. 2), there is also excessive precipitation over northwestern Eurasia (black box in Fig. 9a). This region received more precipitation during June 1993 than in any other June of the last four decades (Fig. 9b), apparently reflecting the impact of the pronounced stationary wave that developed there that month (Fig. 2). We now examine this with our AGCM replay results. The first issue to be addressed is whether any of our replay simulations reproduce the record precipitation anomalies and concomitant circulation anomalies in that region.

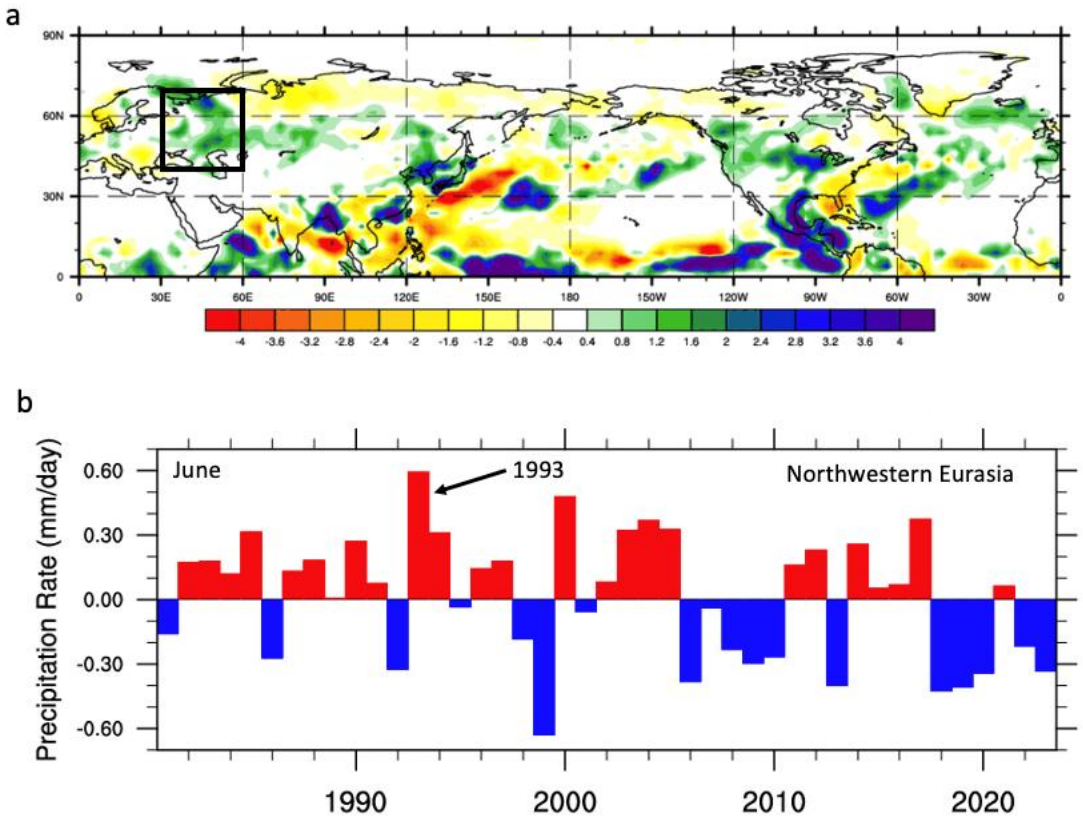

506

507 Figure 9: a. The 1993 June Northern Hemisphere precipitation anomalies (mm/day). b. The June
508 precipitation anomalies (mm/day) averaged between (40°N-70°N, 30°E-60°E, see black box in a)
509 for 1981 through 2023. The precipitation data are from GPCP V2.3 (Adler et al. 2016). The
510 climatology used to produce the anomalies spans the years 1991-2020. Images provided by the
511 NOAA-ESRL Physical Sciences Laboratory, Boulder Colorado from their Web site at
512 https://psl.noaa.gov/.

513

514 This is addressed in section S4 (see Fig. S4.1) where we show results for the individual ensemble
515 members, highlighting the fact that for both NORPL and RPL_TR the observed precipitation
516 anomaly over western Eurasia (see box in Fig. 9a) is a highly unlikely event. In contrast, replaying
517 the NA region (RPL_NA) makes the observed precipitation anomaly much more likely (the
518 observed value is well within the scatter of the ensemble members). As such we focus next on the
519 ensemble mean RPL_NA results.

520

Fig. 10a shows that a pronounced stationary wave indeed extended across much of northern Eurasia during June 1993. Furthermore, that wave is largely reproduced (though weaker) in the RPL_NA ensemble mean results (Fig. 10d). The MERRA-2 precipitation and 850mb wind anomalies (Fig. 10b) exhibit a wave-like structure (presumably reflecting the upper-level circulation) with the main positive precipitation anomalies occurring within a region of low-level cyclonic circulation anomalies. This basic structure is again largely reproduced in RPL_NA (Fig. 10e). Furthermore, the observed cold T2m anomalies together with a tendency for warm anomalies to the east (Fig. 10c) is also mostly reproduced in RPL_NA (Fig. 10f).

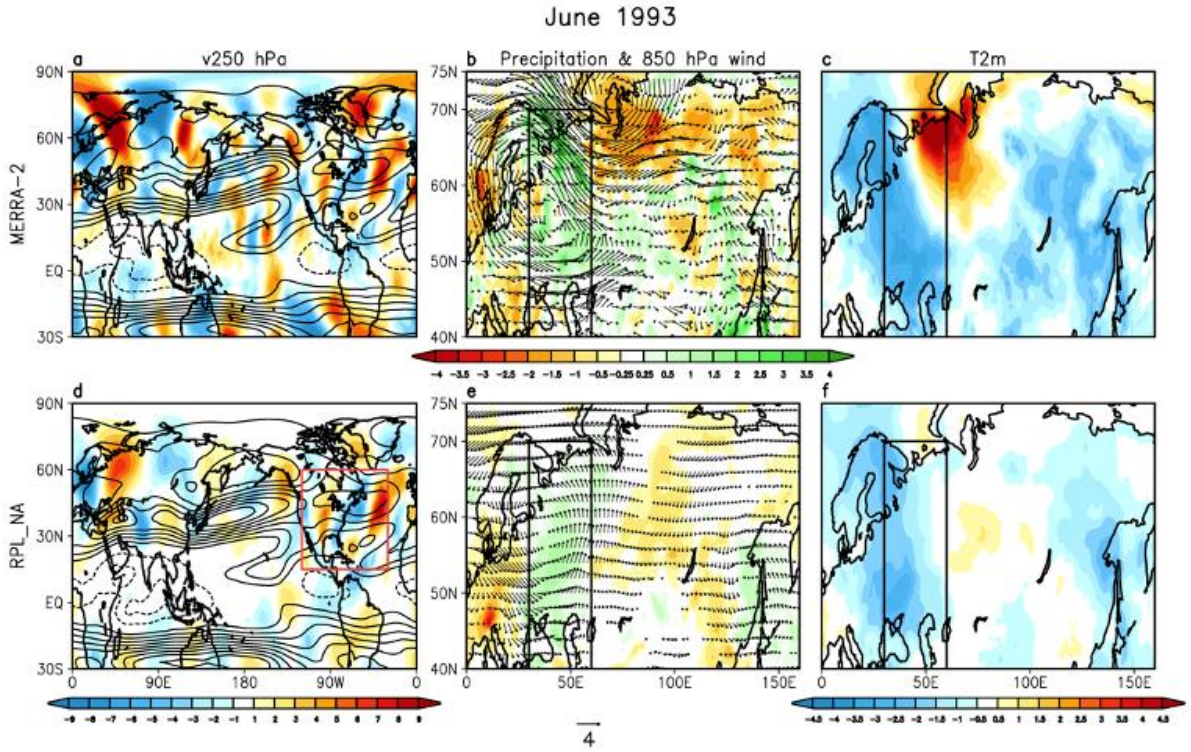

Figure 10: MERRA-2 (top panels) and RPL_NA (bottom panels) results for June 1993. The results are from left to right: 250 hPa v-wind anomalies (m/s) with climatological June 250 hPa u-wind superimposed (contour every 5 m/s, negative dashed and zero omitted), precipitation anomalies (mm/day) with superimposed 850 hPa wind vector anomalies (m/s), and T2m anomalies (°C). The red box in the bottom left panel indicates the RPL_NA replay region. The black boxes outline the region of interest used to produce the scatterplot in Fig. S4.1.

It thus appears from our replay experiments that the key forcing region for that stationary wave is likely somewhere in the NA region. Further insight into the location and nature of the forcing is provided in section S4 employing the SWM. There we show that it was transient vorticity forcing at and just east of the North Atlantic jet exit region that was responsible for forcing the stationary wave. In summary, it thus appears that the active storm track in the North Atlantic produced the pronounced stationary wave that led to the record precipitation over western Eurasia in June.

We next turn to the Midwest July event.

c2. The July event

July was (like June) wet throughout much of the middle latitude land areas (Fig. 11a). Here we focus on the region with excessive precipitation encompassing the northern Great Plains extending westward and northward into Canada (black box in Fig. 11a). This region received by far a record amount of July precipitation during 1993 (Fig. 11b), occurring in conjunction with the pronounced stationary wave that developed there that month (Fig. 2). Here again we determine whether any of our AGCM replay simulations reproduced the record precipitation anomalies and concomitant circulation anomalies in that region.

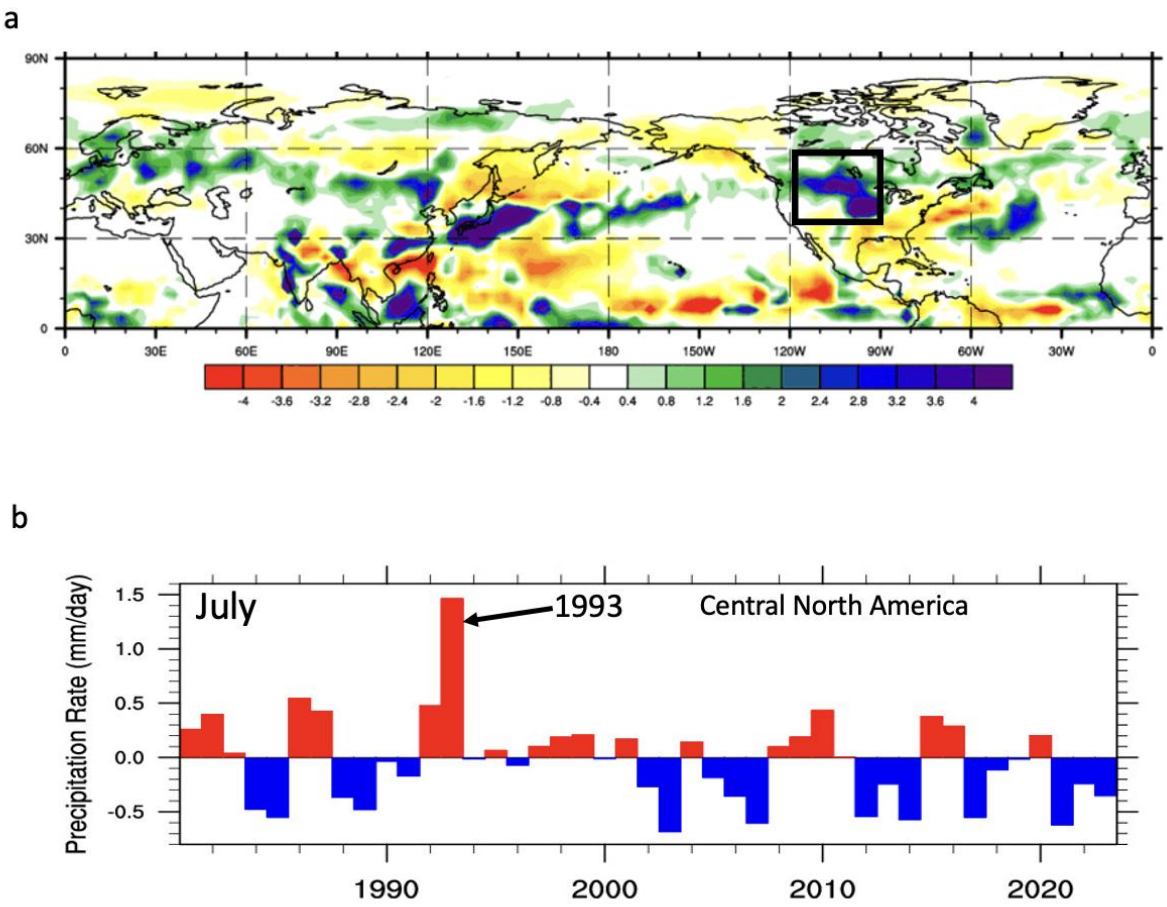

554
555 Figure 11: a. The 1993 July Northern Hemisphere precipitation anomalies (mm/day). b. The July
556 precipitation anomalies (mm/day) averaged between (35°N-60°N, 120°W-90°W, see black box in
557 a) for 1981 through 2023. The precipitation data are from GPCP V2.3 (Adler et al. 2016). The
558 climatology used to produce the anomalies spans the years 1991-2020. Images provided by the
559 NOAA-ESRL Physical Sciences Laboratory, Boulder Colorado from their Web site at
560 https://psl.noaa.gov/.

561

562 Fig. 12 shows a scatterplot of precipitation versus T2m anomalies averaged over the region
563 outlined in Fig. 11a for our various AGCM simulations. In this case, in addition to the NORPL
564 and RPL_TR runs, we examine the results for RPL_CNP– a region in the North Pacific that is just
565 upstream of our North American region of interest. Neither NORPL nor RPL_TR produce
566 significant positive precipitation anomalies in the ensemble mean, though both (especially
567 NORPL) show a tendency for cold anomalies. Focusing on RPL_CNP we see a major shift in the

568 scatter into the lower right quadrant, with the most extreme members approaching the observed
569 precipitation anomaly. Forcing in the CNP region thus appears to be important.

570

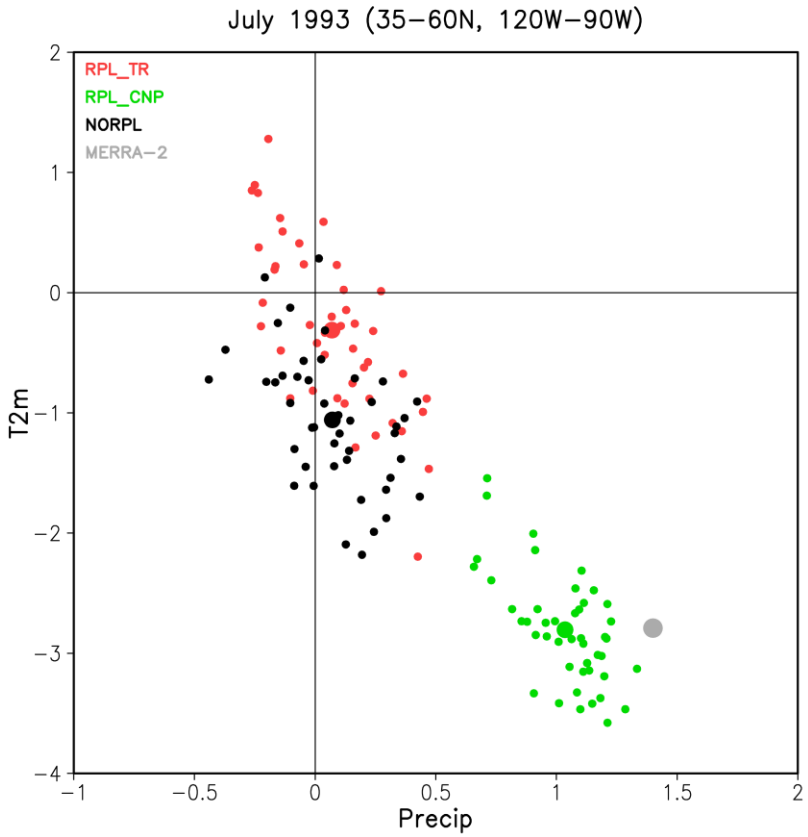

571

572 Figure 12: a. Scatterplot of the July 1993 precipitation (mm day^{-1}) versus T2m (°C) averaged over
573 the North American flood region (35°N-60°N, 120°W-90°W, see black box in Fig. 11a) for all the
574 ensemble members (45) of the model runs (RPL_TR in red, RPL_CNP in green, NORPL in black).
575 The small dots are the individual ensemble members and the large dots are the ensemble means
576 and MERRA-2 (in grey) results.

577

578 Fig. 13 compares the RPL_CNP ensemble mean results with MERRA-2. MERRA-2 shows a
579 pronounced stationary wave in the 250hPa v-wind extending from the eastern North Pacific across
580 North America and into the North Atlantic (Fig. 13a). Over North America this coincides with
581 strong southwesterly 850 hPa winds in the central U.S. – winds that are especially strong in the

582 northern Great Plains where they coincide with the pronounced positive precipitation anomalies
583 in that region (Fig. 13b). The strong southerly wind anomalies reflect an intensification of the
584 GPLLJ and enhanced low-level moisture transport deemed key to producing the extreme
585 precipitation in the upper Midwest during July (e.g., Mo et al. 1995; Bosilovich and Sun 1999;
586 Weaver et al. 2009). Those southerly winds are part of an overall anticyclonic circulation anomaly
587 over the southeast U.S. and a cyclonic circulation anomaly to the north/northwest where it
588 coincides with a secondary positive precipitation anomaly that extends into the Canadian Prairies
589 (Fig. 13b). The cyclonic anomaly also coincides with the coldest T2m temperature anomalies that
590 span much of the upper U.S. and southern Canada west of the Great Lakes (Fig. 13c). Overall, the
591 low level wind anomalies appear to be in phase with the upper level winds, suggesting a generally
592 barotropic structure to the stationary wave (Fig. 13a).

593 The results for RPL_CNP (second row of Fig. 13) show similar features, though with somewhat
594 weaker amplitude. These include the stationary wave (Fig. 13d) and the enhanced southwesterly
595 low level winds in the central U.S. that coincide with positive precipitation anomalies in the upper
596 Midwest (Fig. 13e). There is also a signature of the cyclonic circulation anomaly and associated
597 positive precipitation anomalies that extend into southern Canada, as well as the cold anomalies
598 spanning much of the upper U.S. and southern Canada (cf. Figs. 13c and 13f).

599 Given these results, it is very likely that the forcing of the stationary wave lies somewhere in the
600 central North Pacific (the CNP replay region). So, we again turn to the SWM to better pinpoint
601 the upstream forcing region as well as determine the nature of the forcing (vorticity or heating).

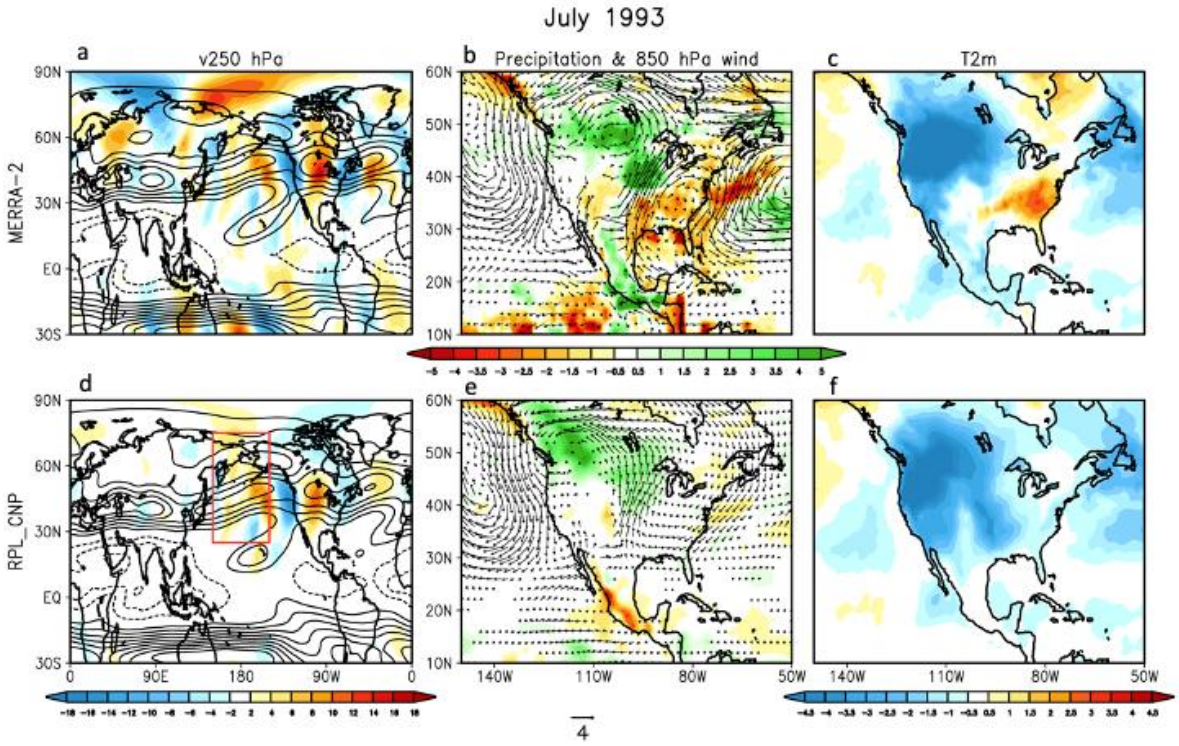

602

603 Figure 13: MERRA-2 (top panels) and RPL_CNP (bottom panels) results for July 1993. The
604 results are from left to right: 250 hPa v-wind anomalies (m/s) with climatological July 250 hPa u-
605 wind superimposed (contour every 5 m/s, negative dashed and zero omitted), precipitation
606 anomalies (mm/day) with superimposed 850 hPa wind vector anomalies (m/s), and T2m anomalies
607 (°C). The red box in panel d indicates the RPL_CNP replay region.

608

609 Before examining the SWM results we should say something about our choice of the basic state
610 for the SWM calculations. The most obvious choice here would be to use the full three-
611 dimensional climatological July basic state (for June, we did use the full three-dimensional
612 climatological June state). It provides the most relevant background flow upon which the July
613 1993 waves can propagate without over specifying the background flow. Having said that, we
614 chose our background state to be the July 1993 zonal mean. We do this because according to a
615 previous study, the 1993 July zonal-mean basic state was conducive to resonance and played a role
616 in the amplification of that stationary wave (Petoukhov et al. 2013). Indeed, the steep meridional
617 gradients of the unusually strong 1993 zonal-mean jet are likely to be more important than any
618 climatological zonal asymmetries in the basic state for trapping and amplifying the quasi-

619 stationary wave. Section S5 provides a limited assessment of the sensitivity of the SWM results
620 to the July basic state.

621 Focusing the SWM analysis on the observed upper tropospheric stream function anomalies
622 encompassed by the black box in Fig. 14c, Figs. 14a and 14b provide, respectively, the resulting
623 sensitivity maps for vorticity and heat. For both forcings, the sensitivity pattern for producing
624 such a stationary wave response consists of wavelike structures oriented in a southwest/northeast
625 direction spanning much of the North Pacific. For vorticity, the largest sensitivity occurs to the
626 north and east of the dateline (along the southern half of the zonal-mean jet) where the pattern
627 forms a positive/negative dipole extending from just northeast of Hawaii to the west coast of North
628 America. For heating, the largest sensitivity has a somewhat similar wave structure, though it is
629 more confined to the eastern North Pacific.

630 Fig. 14d shows that the SWM when forced by the idealized vorticity weighted by the sensitivity
631 does again (as we saw for June) reproduce the observed response (cf. Figs. 14c and 14d).
632 Comparing the sensitivity maps with the actual vorticity and heat forcing (from MERRA-2) shows
633 little overlap for the heating (cf. Figs. 14b and 14f) but considerable overlap for the vorticity (cf.
634 Figs. 14a and 14e), suggesting again that the transient vorticity forcing, with positive forcing to
635 the north and east of Hawaii, is likely most responsible for forcing the stationary wave.
636 Accordingly, the most relevant forcing does indeed appear to lie within the CNP region.

637

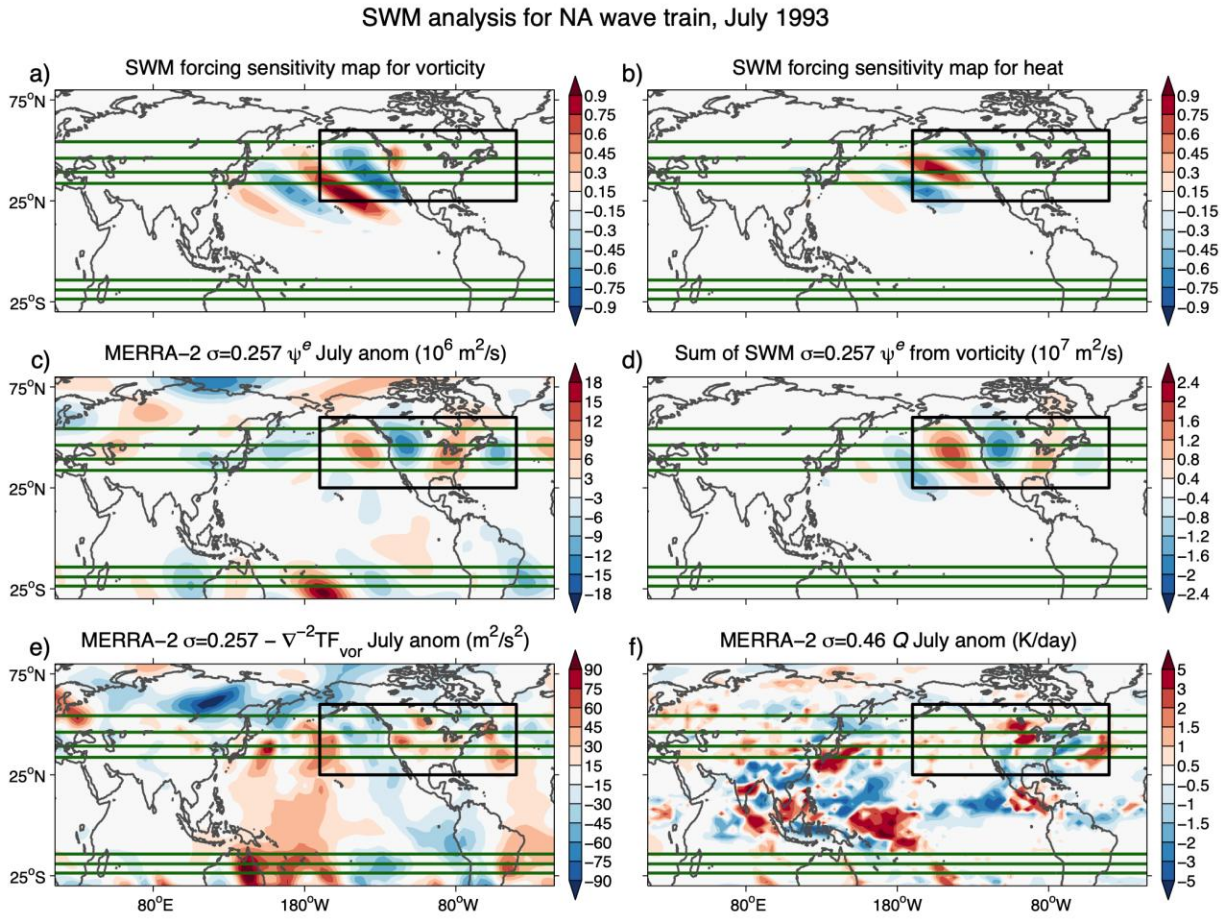

638

639 Figure 14: Results of the stationary wave model (SWM) vorticity and heating experiments
640 targeting the July 1993 stationary wave (outlined by the black box in panel c). The basic state is
641 the July 1993 zonal mean. a. The sensitivity map (**s**) for vorticity forcing (shaded). b. As in (a) but
642 for heat forcing (shaded). c. The observed July 1993 ψ^e anomaly from MERRA-2 interpolated to
643 σ=0.257 (10^6 m^2/s). d. Reconstruction of the observed target ψ^e anomalies at σ=0.257 (10^7 m^2/s),
644 computed by scaling the SWM response maps to vorticity forcing (each associated with a specific
645 forcing location) by the forcing sensitivity at the corresponding forcing locations (shown in panel
646 a) and then summing them. e. The July 1993 transient vorticity forcing (negative of the inverse
647 Laplacian, see text) based on MERRA-2, interpolated to σ=0.257 (m^2/s^2). f) The estimated July
648 1993 diabatic heating (*Q*, K/day) in the mid-troposphere (σ=0.46) based on MERRA-2. In all
649 panels, the straight lines denote the upper tropospheric (σ=0.257) July 1993 zonal-mean u-wind
650 based on MERRA-2 (contour interval is 10 m/s), and the boxes outline the target region.

651

652 In summary, both the June and the July events (in particular the stationary waves key to producing
653 the unusually wet conditions over western Eurasia and central North America) were initiated by

upstream anomalous transient vorticity forcing that occurred within unusually strong zonal wind environments.

4. Summary and Conclusions

In this study we have revisited the cause of the 1993 U.S. Midwest flooding event. Our purpose was in part to clarify some remaining uncertainties about the relative roles of tropical and extratropical forcing, and in part to provide a spatially and temporally broader perspective on the flooding which occurred in a year of multiple spring and summer extremes, some of which occurred in regions far from the Midwest. These include an unusually cold spring Pacific warm pool, a record deep spring Aleutian Low, a record strong June/July NH middle latitude zonal-mean jet, and record June/July wet conditions that spanned much of the Northern Hemisphere middle latitude land areas. Specifically, our results, summarized below, address the following questions 1) what drove the anomalous spring (MAM) precursor environment, and 2) how that environment facilitated the development of the two pronounced stationary waves that produced record rainfall over western Eurasia in June and over the U.S. Midwest in July. Our results also provide some insight into what made the U.S. Midwest flooding such a singular extreme event – still considered extreme today, three decades later.

Here we show that the record springtime Aleutian low was part of a deep North Pacific wave response to strong precipitation/heating anomalies in the equatorial Pacific just west of the dateline. The unusual nature of those springtime tropical precipitation anomalies (just west of the dateline) and the associated atmospheric response can be traced to two factors. First, there is the unusual nature of the tropical Pacific SST anomalies, which were tied to a short-lived, weak, and unusually-timed El Niño (forced in January by a strong MJO event, Delcroix et. al. 2000), and the unusually cold Pacific warm pool SST (a likely lingering impact of the June 1991 Pinatubo eruption, Ward et al. 2021). Second, our GEOS coupled model predictions indicate that the MAM atmospheric response to those SST anomalies (a response that in nature was largely confined to the western Pacific) appears to reflect one of two possible coupled outcomes, with the other characterized by an atmospheric response largely confined to the eastern North Pacific – something more typical of a medium to strong El Niño event. Of the eight coupled

hindcasts initialized in January and February of 1993, four did produce a MAM response in the western/central North Pacific. One hindcast in particular (initialized on January 16) produced a remarkably skillful forecast of the MAM precipitation and circulation anomalies. We speculate (see section S2) that those results reflect two different Bjerknes feedback regimes possible under weak El Niño conditions. It is unclear from our limited sample of hindcasts, however, whether anything systematic in the initial conditions would allow us to predict which of those responses would occur.

While the above results point to the importance of the tropical heating just west of the dateline for generating the extreme atmospheric response in the North Pacific during MAM, it is important to note that internal atmospheric variability also played a role. This is highlighted by the intra-ensemble variability in our 45 tropical replay runs (Fig. 5), which show that even if the tropics are essentially perfectly known, there is still considerable intra-ensemble variability in the extratropical response.

The springtime response in the North Pacific set the stage for the subsequent wet conditions that developed throughout the NH middle latitudes during June and July in the following ways. First, very cold tropospheric temperatures in the North Pacific (between 30°N-50°N) associated with the above-mentioned MAM wave response persisted into June and July. Those cold June/July temperatures were supported at the surface by unusually cold summer SST anomalies that developed in the North Pacific between 30°N-40°N in the vicinity of the strong surface westerly anomalies (associated with the deep Aleutian low). The strong SST gradients in the North Pacific facilitated the development of the enhanced jet (see below) and the baroclinic waves that eventually impacted the US Midwest in June.

While the above MAM wave response was largely confined to the North Pacific, the expansion of the enhanced jet and eddy activity to eventually encompass the entire NH middle latitudes in June and July was facilitated by several factors. First, the mean annual cycle played a role, with the seasonal progression from a springtime jet predominately confined to the western North Pacific to the summertime more longitudinally-uniform jet. This facilitated the propagation of waves/eddies around the globe during June and July. The zonal-mean jet was enhanced during

June and July through feedbacks with both the transient and stationary eddies. In fact, it was primarily the stationary eddies that produced the enhancement and equatorward shift of the zonal-mean jet – eddies that were themselves trapped within the jet wave guide. The enhanced transient eddies did, however, play a critical role in forcing (via transient vorticity forcing) two pronounced stationary waves –one in June anchored over northern Eurasia, and another in July anchored over the Pacific/North American region, resulting in the record precipitation anomalies over northwestern Eurasia and the Northern Great Plains, respectively. As such, the transient waves, by forcing those stationary waves, also had an (indirect) impact on the jet.

With this in mind, we can now address the unresolved issues and/or conflicting results from previous studies concerning the relative contributions to the Midwest flooding of forcing from the tropics and midlatitudes. We have shown that while both the tropics and midlatitudes do in fact play a role, their influence occurred at different times during the course of the spring and summer. *Tropical forcing*, in particular the precipitation/heating anomalies in the tropical Pacific just west of the dateline, was key to forcing the *springtime* wave response in the North Pacific that set the stage for the subsequent summer anomalies (consistent with Bell and Janowiak 1995). Tropical forcing does not appear to have played a direct role in the following months (June/July), given that the weak El Niño had essentially ended by June, and the seasonal expansion of the tropical easterlies would tend to suppress any wave response propagating into the middle latitudes. *Middle latitude forcing* was key to driving events during *June and July*. In particular, the transients (weather systems) did play a role as generally agreed upon in previous studies (e.g., Mo et al. 1995; Trenberth and Guillemot 1996), though their role in June differed from that in July. During June they (the weather systems) had a direct impact on the precipitation over the Midwest as already well documented (e.g., Bell and Janowiak 1995). It is during July, however, that they had the biggest impact on the Midwest by forcing (via anomalous transient vorticity forcing in the North Pacific) the pronounced stationary wave over North America (consistent with Liu et al. 1998), that facilitated the record precipitation over the US Midwest during that month. And again, the transients also played a direct role in forcing the enhanced NH jet during both June and July, though we have found that it was the stationary (monthly mean) eddies that provided most of the forcing of the anomalous jet.

While we have not addressed the potential role of land feedbacks, the soil was clearly already quite wet during June and thus certainly amplified the July flooding (e.g., Kunkel et al. 1994); it seems unlikely however that they had a substantial impact on the main circulation anomalies (e.g., Weaver et al. 2009). On the other hand, the fact that the GEOS AGCM (even when given the correct forcing in the central North Pacific) did not fully reproduce the extreme precipitation that fell over the Midwest during July indicates that possible land feedbacks deserve further investigation.

Finally, we can now also provide some insight into what made the 1993 Midwest flooding such a singular extreme event. In particular, our results suggest that the sequence of events leading to the US Midwest Great Flood had its origins in both the 1991 Pinatubo eruption (via its impact on the Pacific warm pool) and a pronounced January 1993 MJO that initiated the late winter/early spring El Niño event. Furthermore, this occurred in a Pacific climate regime (which ended in 1998/99) during which the boreal spring tropical Pacific SST anomalies were more likely (compared to recent decades) to produce a cyclonic circulation response over the North Pacific - something that helped set the stage for the subsequent 1993 summer flooding event. Clearly, such a combination of events, in the presence of substantial internal atmospheric variability, is unlikely to be repeated in the foreseeable future.

Acknowledgments

This work was supported by the NASA MAP (NNG17HP01C and 80NSSC21K1729) program and the National Climate Assessment Enabling Tools project at NASA's Global Modeling and Assimilation Office (GMAO). MERRA-2 data were developed by the NASA GMAO at the Goddard Space Flight Center (GSFC) under funding by the NASA MAP program. The file specifications for the MERRA-2 output are documented in Bosilovich (2015). The various MERRA-2 fields used for this study (GMAO 2015a; 2015b; 2015c; 2015d) include precipitation that is corrected with gauge and satellite observations (Reichle et al. 2017). Computational resources supporting this work were provided by the NASA High-End Computing (HEC) Program through the NASA Center for Climate Simulation (NCCS) at GSFC.

Data availability statement

MERRA-2 data are available from the Goddard Earth Science Data and Information Services Center (GES DISC) at https://disc.gsfc.nasa.gov. Output from the AGCM simulations can be made available upon request.

784

785 **References**

786 Adler, R., Wang, J.J., Sapiano, M., Huffman, G., Chiu, L., Xie, P.P., Ferraro, R., Schneider, U.,
787 Becker, A., Bolvin, D., Nelkin, E., Gu, G., and NOAA CDR Program (2016). Global
788 Precipitation Climatology Project (GPCP) Climate Data Record (CDR), Version 2.3 (Monthly).
789 National Centers for Environmental Information. DOI: 10.7289/V56971M6
790
791 Bell, G. D., and J. E. Janowiak, 1995: Atmospheric Circulation Associated With the Midwest
792 Floods of 1993. Bull. Amer. Meteor. Soc., 76, 681–696, https://doi.org/10.1175/1520-
793 0477(1995)076<0681:ACAWTM>2.0.CO;2.
794
795 Bosilovich, M. G., and W. Sun, 1999: Numerical Simulation of the 1993 Midwestern Flood:
796 Land–Atmosphere Interactions. J. Climate, 12, 1490–1505, https://doi.org/10.1175/1520-
797 0442(1999)012<1490:NSOTMF>2.0.CO;2.
798
799 Bosilovich, M. G., 2015: *GMAO Office Note No. 9 (Version 1.1)*: MERRA-2: File Specification.
800 Available at https://gmao.gsfc.nasa.gov/pubs/
801

802 Chang, Y., S.D. Schubert, R.D. Koster, A.M. Molod, and H. Wang, 2019: Tendency Bias
803 Correction in Coupled and Uncoupled Global Climate Models with a Focus on Impacts over
804 North America. *J. Climate,* **32**, 639–661.

805
806 Climate Analysis Center (1994): Fifth Annual Climate Assessment 1993. M.S. Halpert, G.D.
807 Bell, V.E. Kousky, and C.F. Ropelewski, editors. Department of Commerce, NOAA/NWS/NMC,
808 Climate Analysis Center, 111 pp.
809
810 DeAngelis, A. M., S. D. Schubert, Y. Chang, Y. Lim, R. D. Koster, H. Wang, and A. B. Marquardt
811 Collow, 2023: Dynamical drivers of the exceptional warmth over Siberia during the spring of
812 2020. *J. Climate*, **36**, 4837–4861, https://doi.org/10.1175/JCLI-D-22-0387.1.

Delcroix, T., B. Dewitte, Y. duPenhoat, F. Masia, and J. Picaut (2000), Equatorial waves and warm pool displacements during the 1992–1998 El Niño Southern Oscillation events: Observation and modeling, J. Geophys. Res., 105(C11), 26045–26062, doi:10.1029/2000JC900113.

Edmon , H. J., Jr., Hoskins, B. J., & McIntyre, M. E. (1980). Eliassen-Palm Cross Sections for the Troposphere, Journal of Atmospheric Sciences, 37(12), 2600-2616.

Eliassen, A. and E. Palm, 1961: On the transfer of energy in stationary mountain waves. *Geofys. Publ.*, **22**, 1-23.

Gelaro, R., W. McCarty, M.J. Suárez, R. Todling, A. Molod, L. Takacs, C.A. Randles, A. Darmenov, M.G. Bosilovich, R. Reichle, K. Wargan, L. Coy, R. Cullather, C. Draper, S. Akella, V. Buchard, A. Conaty, A.M. da Silva, W. Gu, G. Kim, R. Koster, R. Lucchesi, D. Merkova, J.E. Nielsen, G. Partyka, S. Pawson, W. Putman, M. Rienecker, S.D. Schubert, M. Sienkiewicz, and B. Zhao, 2017: The Modern-Era Retrospective Analysis for Research and Applications, Version 2 (MERRA-2). *J. Climate,* 30, 5419–5454.

GMAO, 2015a: tavg1_2d_slv_Nx: 2d, 1-hourly, time-averaged, single-level, assimilation, single-level diagnostics, V5.12.4. Goddard Space Flight Center Distributed Active Archive Center (GSFC DAAC), accessed 1 February 2023, https://doi.org/10.5067/VJAFPLI1CSIV.

GMAO, 2015b: tavg1_2d_flx_Nx: 2d, 1-hourly, time-averaged, single-level, assimilation, surface flux diagnostics, V5.12.4. Goddard Space Flight Center Distributed Active Archive Center (GSFC DAAC), accessed 1 February 2023, https://doi.org/10.5067/7MCPBJ41Y0K6.

GMAO, 2015c: inst3_3d_asm_Np: 3d, 3-hourly, instantaneous, pressure-level, assimilation, assimilated meteorological fields, V5.12.4. Goddard Space Flight Center Distributed Active Archive Center (GSFC DAAC), accessed 1 February 2023, https://doi.org/10.5067/QBZ6MG944HW0.

GMAO, 2015d: tavg3_3d_tdt_Np: 3d, 3-hourly, time-averaged, pressure-level, assimilation, temperature tendencies, V5.12.4. Goddard Space Flight Center Distributed Active Archive Center (GSFC DAAC), accessed 1 February 2023, https://doi.org/10.5067/9NCR9DDDOPFI.

Griffies, S. (2012). Elements of the Modular Ocean Model (MOM). http://mdl-mom5.herokuapp.com/web/docs/project/MOM5_elements. Pdf.

Griffies, S., Gnanadesikan, A., Dixon, K. W., Dunne, J. P., Gerdes, R., Harrison, M. J., et al. (2005). Formulation of an ocean model for global climate simulations. Ocean Science, 1, 1025–1035.

Huang, B., P. W. Thorne, V. F. Banzon, T. Boyer, G. Chepurin, J. H. Lawrimore, M. J. Menne, T. M. Smith, R. S. Vose, and H.-M. Zhang, 2017: Extended Reconstructed Sea Surface Temperature, version 5 (ERSSTv5): Upgrades, validations, and intercomparisons. J. Climate, 30, 8179-8205, doi:10.1175/JCLI-D-16-0836.1.

Koster, R. D., Suarez, M. J., Ducharne, A., Stieglitz, M., & Kumar, P. (2000). A catchment-based approach to modeling land surface processes in a GCM, Part 1, Model structure. Journal of Geophysical Research, 105, 24,809–24,822. https://doi.org/10.1029/2000JD900327.

Kunkel, K. E., S. A. Changnon, and J. R. Angel, "Climatic aspects of the 1993 Upper Mississippi River Basin flood," Bulletin of the American Meteorological Society, vol. 75, no. 5, pp. 811–822, 1994.

Lee, S., L'Heureux, M., Wittenberg, A.T. *et al.* On the future zonal contrasts of equatorial Pacific climate: Perspectives from Observations, Simulations, and Theories. *npj Clim Atmos Sci* **5**, 82 (2022). https://doi.org/10.1038/s41612-022-00301-2

873 Liu, A. Z., M. Ting, and H. Wang, “Maintenance of circulation anomalies during the 1988
874 drought and 1993 floods over the United States,” Journal of the Atmospheric Sciences, vol. 55,
875 no. 17, pp. 2810–2832, 1998.
876
877 Lyon, B., A. G. Barnston, and D. G. DeWitt, 2013: Tropical pacific forcing of a 1998–1999
878 climate shift: Observational analysis and climate model results for the boreal spring season.
879 Climate Dyn., 43, 893–909, doi:10.1007/s00382-013-1891-9.
880
881 Mo, K. C., Nogues-Paegle, J., & Paegle, J. (1995). Physical Mechanisms of the 1993 Summer
882 Floods, Journal of Atmospheric Sciences, 52(7), 879-895.
883
884 Molod, A. M., L. Takacs, M. Suarez, and J. Bacmeister, 2015: Development of the GEOS-5
885 atmospheric general circulation model: evolution from MERRA to MERRA2. *Geosci. Model Dev.*,
886 8, 1339-1356, doi:10.5194/gmd-8-1339-2015.
887
888 Molod, A., E. Hackert, Y. Vikhliaev, B. Zhao, D. Barahona, G. Vernieres, A. Borovikov, R. M.
889 Kovach, J. Marshak, S. Schubert, Z. Li, Y.-K. Lim, L. C. Andrews, R. Cullather, R. Koster, D.
890 Achuthavarier, J. Carton, L. Coy, J. L. M. Freire, K. M. Longo, K. Nakada, and S. Pawson, 2020.
891 GEOS-S2S Version 2: The GMAO High Resolution Coupled Model and Assimilation System
892 for Seasonal Prediction. J. Geophy. Res. - Atmos., 125, e2019JD031767. doi:
893 10.1029/2019JD031767
894
895 Petoukhov,V., S Rahmstorf, S Petri, HJ Schellnhuber, Quasiresonant amplification of planetary
896 waves and recent Northern Hemisphere weather extremes. *Proc Natl Acad Sci USA* **110**, 5336–
897 5341 (2013).
898
899 Reichle, R. H., Q. Liu, R. D. Koster, C. S. Draper, S. P. P. Mahanama, and G. S. Partyka (2017),
900 Land surface precipitation in MERRA-2. *Journal of Climate*, 30, 1643-1664, doi: 10.1175/JCLI-
901 D-16-0570.1.
902

Rienecker, M. M., Rienecker, M. M., Todling, R., Bacmeister, J., Takacs, L., Liu, H. C., et al. (2008). The GEOS-5 data assimilation system: Documentation of versions 5.0.1 and 5.1.0, and 5.2.0 (NASA Tech. Rep.): Series on Global Modeling and Data Assimilation NASA/TM-2008-104606.

Schubert, S., Wang, H., & Suarez, M., 2011: Warm Season Subseasonal Variability and Climate Extremes in the Northern Hemisphere: The Role of Stationary Rossby Waves, Journal of Climate, 24(18), 4773-4792. Retrieved Apr 28, 2022, from https://journals.ametsoc.org/view/journals/clim/24/18/jcli-d-10-05035.1.xml

Schubert, S., A. Borovikov, Y-K. Lim, and A. Molod, 2019a: Ensemble Generation Strategies Employed in the GMAO GEOS-S2S Forecast System. *Technical Report Series on Global Modeling and Data Assimilation,* Randal D. Koster, editor. NASA/TM-2019-104606, Vol. 53, 65 pp.

Schubert, S. D., Y. Chang, H. Wang, R. D. Koster, and A. M. Molod, 2019b. A Systematic Approach to Assessing the Sources and Global Impacts of Errors in Climate Models. J. Climate, 32, 8301-8321. doi: 10.1175/JCLI-D-19-0189.1.

Schubert, S.D, Y. Chang, A. M. DeAngelis, H. Wang, and R.D. Koster, 2021: On the Development and Demise of the Fall 2019 Southeast U. S. Flash Drought: Links to an Extreme Positive IOD, *J.* Climate, 34(5), 1701-1723.

Schubert, S.D., Y. Chang, A.M. DeAngelis, R. D. Koster, Y.-K. Lim, and Hailan Wang, 2022: Exceptional Warmth in the Northern Hemisphere during January through March of 2020: The Roles of Unforced and Forced Modes of Atmospheric Variability, J. Climate, 35 (8), 2565-2584.

Schubert, Siegfried D., Yehui Chang, Anthony M. DeAngelis, Young-Kwon Lim, Natalie P. Thomas, Randal D. Koster, Michael G. Bosilovich, Andrea M. Molod, Allison Collow, Amin Dezfuli, 2024: Insights into the Causes and Predictability of the 2022/23 California Flooding, *J. Climate*, **37**, 3613–3629, https://doi.org/10.1175/JCLI-D-23-0696.1.

Smith C. A., G. P. Compo and D. K. Hooper (November 2014): Web-Based Reanalysis Intercomparison Tools (WRIT) for Analysis and Comparison of Reanalyses and Other Datasets. Bull. Am. Meteorol. Soc., 95 (11), 1671-1678. doi:10.1175/BAMS-D-13-00192.1

Ting, M., and L. Yu, 1998: Steady Response to Tropical Heating in Wavy Linear and Nonlinear Baroclinic Models. J. Atmos. Sci., 55, 3565–3582, https://doi.org/10.1175/1520-0469(1998)055<3565:SRTTHI>2.0.CO;2.

Trenberth, K. E. and C. J. Guillemot, 1996: Physical processes involved in the 1988 drought and 1993 floods in north America, Journal of Climate, vol. 9, no. 6, pp. 1288–1298.

Trenberth, K.E., and J.W. Hurrell, 1994: Decadal atmosphere-ocean variations in the Pacific. Climate Dynamics 9, 303–319. https://doi.org/10.1007/BF00204745

Wang, H., and M. Ting, 1999: Seasonal Cycle of the Climatological Stationary Waves in the NCEP–NCAR Reanalysis. J. Atmos. Sci., 56, 3892–3919, https://doi.org/10.1175/1520-0469(1999)056<3892:SCOTCS>2.0.CO;2.

Ward, B., Pausata, F. S. R., & Maher, N. (2021). The sensitivity of the El Ninõ-Southern Oscillation to volcanic aerosol spatial distribution in the MPI Grand Ensemble. *Earth System Dynamics*, *12*(3), 975-996. https://doi.org/10.5194/esd-12-975-2021

Weaver, S. J., A. Ruiz-Barradas, and S. Nigam, "Pentad evolution of the 1988 drought and 1993 flood over the great plains: an NARR perspective on the atmospheric and terrestrial water balance," Journal of Climate, vol. 22, no. 20, pp. 5366–5384, 2009.

Zhang, Yu & Xie, Shang-Ping & Kosaka, Yu & Yang, Jun-Chao. (2018). Pacific Decadal Oscillation: Tropical Pacific Forcing versus Internal Variability. Journal of Climate. 31. 10.1175/JCLI-D-18-0164.1.